Contents lists available at ScienceDirect

Acta Materialia

journal homepage: www.elsevier.com/locate/actamat

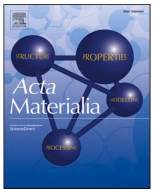

Effect of Dislocation Character on the CRSS

Orcun Koray Celebi, Ahmed Sameer Khan Mohammed, Huseyin Sehitoglu [*]

Department of Mechanical Science and Engineering, University of Illinois at Urbana-Champaign, 105 S. Mathews Ave., Urbana, IL 61801, USA

ARTICLE INFO

Keywords:
Dislocations
Core width
Peierls stress
Stacking fault
Wigner-Seitz cell

ABSTRACT

The yield strength of a crystalline structural material is a fundamental mechanical property predominantly governed by the critical stress for dislocation slip. This Critical Resolved Shear Stress (CRSS) is strongly influenced by the character of the dislocation (e.g., screw, edge, or mixed) as shown in previous experimental studies. Existing analytical approaches for CRSS prediction assume an atomic row description of the slip plane and do not account for Wigner-Seitz (WS) cell area at each discrete lattice site. Further, inadequate consideration of the material's elastic anisotropy and the presumed dislocation "core-width" level precludes correct CRSS determination. This study proposes a predictive model applied to Face Centered Cubic (FCC) materials addressing these shortcomings in predicting glide stress of a dissociated dislocation. The core-width is rigorously determined from the minimization of total energy comprised of continuum strain energy (E_{STRAIN}) and atomistic misfit energy (E_{MISFIT}) of the dislocation's core. The E_{STRAIN} is obtained from dislocation strain-fields calculated using the fully-anisotropic Eshelby-Stroh formalism. The E_{MISFIT} is determined from the Generalized Stacking Fault Energy (GSFE) landscape of the slip plane. Previous E_{MISFIT} calculations are restricted to slipped rows in 'simple' cubic lattices which do not represent the slip-planes in FCC crystals. The developed model is used to predict CRSS for a wide range of metallic materials correcting the overprediction of experimental CRSS levels. The results unveiled the remarkable dependence of CRSS on the dislocation character, revealing the non-trivial dependence on GSFE parameters. Thus, this study addresses a major void in structure-property prediction for structural materials.

1. Introduction

Plastic deformation of crystalline materials is largely accommodated by dislocation motion. These dislocations are either pre-existing in the material or nucleate from internal sources. The motion of these defects is controlled by the intrinsic flow resistance, i.e., CRSS which is an essential input to many crystal-plasticity models [1,2]. It governs the dislocation motion in fatigue leading to irreversibilities [3,4] and gages the fracture propensity in ductile/brittle transition [5]. Nonetheless, the field of materials science and mechanics is still lacking a parameter-free CRSS model that internalizes the correct crystallography of the slip-plane. Existing approaches focus primarily on pure dislocation characters (e.g., edge or screw) and adopt the classical methods to calculate the misfit energy of a dislocation for crystals that are not simple cubic [6–12]. However, such a direct transfer of the classical approach, which is originally developed for simple cubic crystals [13,14], fails to capture the lattice-dependent distribution of the discrete atomic positions on the slip-plane. The inaccuracy in this treatment is even more amplified for the dislocations with a mixed character as the correct atomic positions can be described neither by individual treatment of the screw and edge components of the dislocation with the row-misfit approach nor by employing correction factors for core-width determination [7,15]. Further, many of the existing approaches assumed isotropy to circumvent the coupling between the edge and screw components resulting in an inaccurate representation of the mixed dislocations [10,16]. However, mixed dislocations are prevalent and constitute a significant fraction of the total dislocation density in metallic materials [17–19]. Additionally, in the case of Face Centered Cubic (FCC) crystals at least one of the Shockley partials of a dissociated dislocation has a mixed character due to the crystallography of the slip plane. Therefore, there is a need for a more generalized theory that is capable of analyzing different dislocation characters and a wide range of materials where the character effect reflects both the material anisotropy and the misfit energy. In this study, we propose a model that predicts CRSS for a dislocation with an arbitrary character as influenced by the elastic constants, the critical fault energies of the material intrinsically linked to the dislocation core-width. The analysis is free of empirical parameters and is based only on intrinsic lattice-dependent calculations.

---

[*] Corresponding author.
E-mail address: huseyin@illinois.edu (H. Sehitoglu).

https://doi.org/10.1016/j.actamat.2023.118982
Received 4 October 2022; Received in revised form 27 April 2023; Accepted 2 May 2023

1.1. Core structure fundamentals: Disregistry and Dislocation density distributions

The required stress to move the dislocation on its slip plane is primarily related to the intrinsic strength of the material. The onset of glide is achieved when the resolved stress on the dislocation exceeds the intrinsic lattice friction stress [14]. And it is primarily controlled by the core-properties of a dislocation, particularly by the width of the core [13]. It is well known that there is an inverse relationship between the core-width of a dislocation and the friction stress [20]. The size of the core is dominated by the material parameters, and it requires a detailed analysis to obtain the correct core-width of a dislocation. The well-established Peierls model quantitively describes the distribution of the dislocation core via disregistry function [13,14,20]. The disregistry function is solved from the balance of elastic forces due to the strain-field around the dislocation and the restoring atomic forces at the core of the dislocation. The sinusoidal restoring-force assumption yields the commonly used disregistry function for a full dislocation parametrized by the "half core-width" of the dislocation which predominantly dictates the CRSS [6,21]. However, a general robust framework to predict the core-width for a dislocation with an arbitrary character is currently unavailable, to the best of the authors' knowledge, hence precluding a reliable prediction for the CRSS. The limitations of existing approaches are discussed in more detail in the following section and resolved in later sections with the proposed theory.

1.2. Limitations of existing approaches

1.2.1. Mixed dislocation character

Prior studies on this topic focused mainly on edge or screw character dislocations. The vast majority of the spectrum of mixed dislocation characters is undiscovered. However, an arbitrary dislocation line in a material is randomly curved with varying characters along its length. As a consequence, to truly predict the yield strength of such a material, the behavior of the CRSS of the dislocation with an arbitrary character must be determined.

1.2.2. Effect of atomistic fault energies on CRSS

The core energy of the dislocation is governed by the associated fault energy barrier also known as the Generalized Stacking Fault Energy (GSFE) landscape [22]. In the case of FCC materials, the GSFE landscape is described by two critical points, namely, the stable intrinsic stacking fault energy γ_{isf} and the unstable stacking fault energy barrier γ_{us}. The CRSS is strongly dependent upon these critical values as it directly quantifies the core energy of a dislocation. However, this dependence is complex and is initially manifested in the misfit energy of the dislocation. The individual effect of these critical points on the CRSS is not established to date and is unraveled in this study. Many previous studies used the ideal shear-strength, $\tau_{\max}$, to describe the atomistic restoring-force relationship [23–25]. However, with a distributed dislocation core this relation is not accurate because the restoring force is due to the response of the crystal to the planar dislocation core distributed on the slip plane and cannot be described by a constant ideal shear strength, $\tau_{\max}$. Therefore, the entire GSFE curve must be involved in the analysis for accurate calculation of the core energy of a dislocation. This non-trivial dependence of CRSS on the GSFE landscape is unexplored and is unveiled in the current study.

1.2.3. Effect of character on nature of motion

Correct calculation of the CRSS requires the motion of the dislocation to be precisely known as the energy barrier for motion greatly depends on accurate sampling from the GSFE curve corresponding to the relative positions of the Shockley partials. This necessitates the respective positions of Shockley partials to be tracked throughout the motion. Previously, it was thought that the Shockley partials move together such that the fault-width between them stays constant when the barrier for motion is exceeded. In the present study, this assumption is challenged and is shown that energetically more favorable path is much more complex involving a "zig-zag" pattern rather than a simultaneous motion of the partials. To put it concisely, first the leading Shockley partial moves with the trailing partial stationary, which results in an increase in the stacking fault width. Then, the trailing partial follows with the leading partial fixed in position and the stacking fault width restores to its equilibrium value. Therefore, this results in a fluctuation in the stacking fault width as the dislocation moves. The magnitude of this fluctuation varies depending upon the material properties and dislocation characteristics as dictated by the total energy landscape of the extended dislocation.

1.2.4. Effect of changing lattice with character

Existing models employing the Peierls-Nabarro framework inaccurately handled the changing atomic arrangements on the slip-plane depending upon the lattice structure, dislocation character, or the slip system. They employed a one-dimensional row-misfit approach which involves a series summation for misfit-energy using a discrete parameter a' in an effort to capture the periodicity of the lattice. However, correct understanding of the effect of dislocation character requires that the individual atomic-sites on the slip-plane be involved in the analysis. This necessitates two-dimensional consideration of the slip-plane as the atomic arrangements cannot be defined in one-dimension for crystals that are not simple-cubic. As a result, this led to unrealistically high friction stress predictions due to the oversimplification of this complex problem. And other studies recognized this error in representing the correct atom positions across the slip plane and tried to address these unrealistic results by using a correction factor in the commonly used exponential relation [15,26,27]. However, all these approaches failed to address the underlying problem.

1.2.5. Asymmetric core structure of a mixed dislocation

Full dislocations with a pure character (edge or screw) split into two partials, both of which have the same nature. Thus, they have a symmetrical distribution of the core as dislocations with the same characters have the same core-widths. On the other hand, dislocations with a mixed character split into Shockley partials with distinct characters and core-widths. Therefore, mixed dislocations have an asymmetric distribution of the cores, unlike pure dislocations [19]. If the character of the partial is closer to the edge, the dislocation has a much wider core as compared to the screw character which has the smallest core-width amongst all characters. This asymmetry imposes fundamental conditions on how the dislocation moves as the two partials have distinct barriers to glide. Thus, this asymmetry must be inherently incorporated into the theory when calculating the core energy of the dislocation.

1.3. Current approach

The present study addresses all these limitations and establishes an empirical-parameter-free predictive model for the CRSS of FCC materials. The developed framework models the $a/2\langle 011\rangle$ straight extended dislocation of a general mixed character in FCC materials, comprising two $a/6\langle 112\rangle$ Shockley partials separated by a stacking fault of finite width, where a represents the lattice constant of the FCC crystal. In the current study, we adopt an energy-based approach to predict the correct core-structure of a general extended dislocation. The equilibrium core structure of the partials is obtained from total energy minimization consisting of long-range elastic strain energy and short-range misfit energy of a dislocation. We employ a recent method developed by the authors and generalized it for varying dislocation character [28,29]. The elastic energy is calculated by employing the fully anisotropic Eshelby-Stroh (E-S) formalism. The strain field around the dislocation is computed using the E-S parameters, which allows accurate determination of the anisotropic interaction coefficients. The misfit energy is

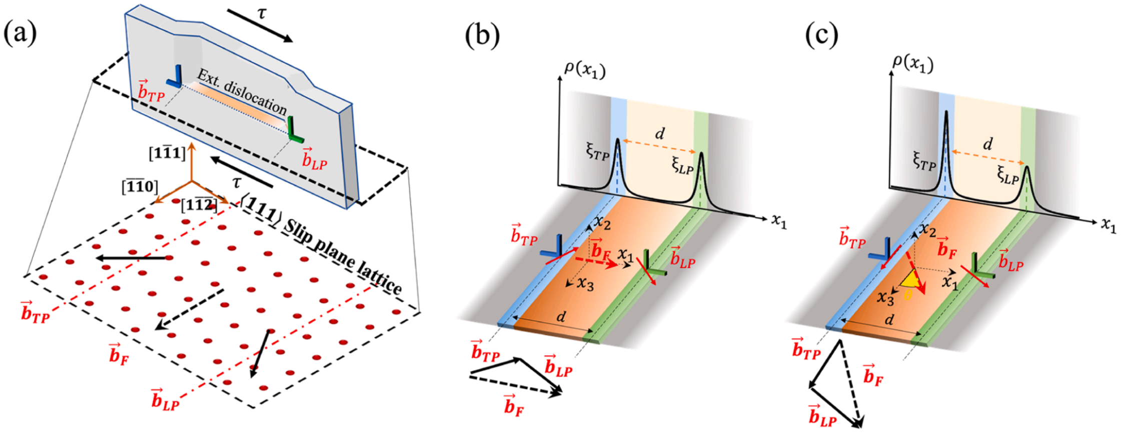

Fig. 1. Dislocation core-structure: (a) extended dislocation and the atomic arrangements on the slip plane along with the directions of the Burgers vectors for the leading and trailing partials and for the full dislocation (screw case shown) (b) the $x_1 - x_2 - x_3$ coordinate system attached to a pure dislocation with Burgers vector $\vec{b}_F$, the dislocation line aligned with the x_3 axis and on the slip plane with normal in the x_2 direction; corresponding symmetric dislocation-density distribution, $\rho(x_1)$, of a dissociated dislocation indicating the core-widths $\xi_{TP,LP}$ of the trailing and leading partials respectively (edge case shown). (c) the x_1 $-x_2$ $-x_3$ coordinate system attached to a mixed dislocation with Burgers vector $\vec{b}_F$, the dislocation line aligned with the x_3 axis and on the slip plane with normal in the x_2 direction; corresponding dislocation-density distribution, $\rho(x_1)$, of a dissociated mixed dislocation indicating the asymmetric core-widths $\xi_{TP,LP}$ of the trailing and leading partials respectively.

computed by utilizing the GSFE landscape of the material by being faithful to the two-dimensional crystal lattice structure on the slip plane. Finally, the minimum energy pathway for the glide of partials on the slip-plane is obtained by independent treatment of the positions of the Shockley partials, subsequently used to calculate the CRSS. The methodology of the predictive framework is presented next.

2. Methodology and Results

2.1. *Core-structure of the $a/2\langle 011\rangle$ extended dislocation*

In FCC materials, full dislocation, $\vec{b}_F$, tends to split into two Shockley partials on the slip plane, a leading partial, $\vec{b}_{LP}$, and a trailing partial, $\vec{b}_{TP}$, since it yields a lower energy structure for the dislocation and reduces dilation and compression on the sides of the slip plane [20, 23]. The extended dislocation consisting of these two partials is illustrated in Fig. 1 (a). Depending upon the character of the parent full dislocation, the Shockley partials admit a certain character. The character of the full dislocation is determined from the angle between the dislocation line and the Burgers vector as shown by θ in Fig. 1 (c). As mentioned, in the case of pure edge and screw dislocations, Shockley partials have the same characters, which results in a symmetric dislocation density distribution on the slip plane as depicted in Fig. 1 (b) for the edge case. On the other hand, for dislocations with a mixed character, the dislocation density distribution is asymmetric due to the distinct characters of the Shockley partials as illustrated in Fig. 1 (c).

In the current analysis, the CRSS is predicted for the $\vec{b}_F = a/2[\bar{1}\bar{1}0]$ dislocation dissociated on the $(1\bar{1}1)$ slip plane. The magnitude of the full dislocation $\vec{b}_F$ is represented by b_F, and for the partials, it is given by b_P. The center of the leading partial's core is located at $x_1 = s_1$, while that of the trailing partial is at $x_1 = s_2$. The fault-width between them is computed by $d = s_1 + s_2$ as demonstrated in Figs. 1 (b, c). Hence, the core-structure of the extended dislocation is described by the disregistry function:

$$f(x_1) = b_P + \frac{b_P}{\pi}\left(\tan^{-1}\left(\frac{x_1 + s_2}{\xi_{TP}}\right) + \tan^{-1}\left(\frac{x_1 - s_1}{\xi_{LP}}\right)\right) \tag{1}$$

The dislocation density distribution $\rho(x_1)$ which is derivative of $f(x_1)$, is given by:

$$\rho(x_1) = \frac{b_P}{\pi}\left(\frac{\xi_{TP}}{(x_1 + s_2)^2 + \xi_{TP}^2} + \frac{\xi_{LP}}{(x_1 - s_1)^2 + \xi_{LP}^2}\right) \tag{2}$$

Burgers vectors for the Shockley partials are in different <121> family directions on the slip-plane as shown in Fig. 1 (a). Thus, accurate representation of the dislocation distributions necessitates the decomposition of this superposed function. This allows us to calculate the necessary energy components, especially the strain energies, more precisely by making a clear distinction between the cores of the two partials which partially overlap in some cases. The decomposition can be described by the relations $f_{TP}(x_1) + f_{LP}(x_1) = f(x_1)$ and $\rho_{TP}(x_1) + \rho_{LP}(x_1) = \rho(x_1)$. Hence, we can write the core disregistry distribution of the leading and trailing partials, and their corresponding dislocation density distributions respectively by the equations:

$$\begin{aligned} f_{TP}(x_1) &= \frac{b_P}{2} + \frac{b_P}{\pi}\tan^{-1}\left(\frac{x_1 + s_2}{\xi_{TP}}\right) \\ \rho_{TP}(x_1) &= \frac{b_P}{\pi}\left(\frac{\xi_{TP}}{(x_1 + s_2)^2 + \xi_{TP}^2}\right) \end{aligned} \tag{3}$$

$$\begin{aligned} f_{LP}(x_1) &= \frac{b_P}{2} + \frac{b_P}{\pi}\tan^{-1}\left(\frac{x_1 + s_1}{\xi_{LP}}\right) \\ \rho_{LP}(x_1) &= \frac{b_P}{\pi}\left(\frac{\xi_{LP}}{(x_1 - s_1)^2 + \xi_{LP}^2}\right) \end{aligned} \tag{4}$$

The Eqs. (3, 4) completely describe the core structure of the extended dislocation as governed by parameters; the core-width ξ_{TP} of the trailing partial, core-width ξ_{LP} of the leading partial, and the stacking fault width $d = s_1 + s_2$. The determination of these parameters using an energy-minimization method is described next.

2.2. *The energy of the extended dislocation: Continuum-strain energy and Atomistic misfit energy*

The total energy of the $a/2\langle 011\rangle$ extended dislocation, E_{TOT}, has two energy constituents: (i) strain energy due to continuum elastic strain-fields introduced by the dislocation, E_{STRAIN}, and (ii) atomistic misfit energy at the core of the dislocation, E_{MISFIT}, due to stretching of the bonds. Hence, this relation is expressed as:

Table 1

Anisotropic interaction coefficients K_{11}, K_{22}, and K_{12} needed to compute the continuum strain-energy of the $a/2\langle 011\rangle$ extended dislocation for Ni (in units of $\times 10^2$ GPa).

Material	Char. angle (θ)	K_{11}	K_{22}	K_{12}
Ni	0°	-0.932	-0.932	-0.666
	6.58°	-0.903	-0.969	-0.679
	8.94°	-0.895	-0.983	-0.689
	13.9°	-0.881	-1.014	-0.719
	23.4°	-0.868	-1.072	-0.799
	30°	-0.867	-1.109	-0.865
	36.58°	-0.866	-1.140	-0.935
	46.09°	-0.881	-1.176	-1.043
	60°	-0.932	-1.198	-1.198
	73.9°	-1.014	-1.176	-1.310
	83°	-1.073	-1.140	-1.346
	90°	-1.109	-1.109	-1.353

Table 2

Anisotropic interaction coefficients K_{11}, K_{22}, and K_{12} needed to compute the continuum strain-energy of the $a/2\langle 011\rangle$ extended dislocation for FeNiCoCrMn (in units of $\times 10^2$ GPa).

Material	Char. angle (θ)	K_{11}	K_{22}	K_{12}
FeNiCoCrMn	0°	-0.862	-0.862	-0.538
	6.58°	-0.834	-0.900	-0.560
	8.94°	-0.828	-0.916	-0.577
	13.9°	-0.823	-0.954	-0.626
	23.4°	-0.827	-1.026	-0.746
	30°	-0.830	-1.069	-0.829
	36.58°	-0.827	-1.106	-0.906
	46.09°	-0.823	-1.150	-1.019
	60°	-0.860	-1.181	-1.180
	73.9°	-0.954	-1.150	-1.282
	83°	-1.026	-1.106	-1.306
	90°	-1.069	-1.069	-1.309

Table 3

Anisotropic interaction coefficients K_{11}, K_{22}, and K_{12} needed to compute the continuum strain-energy of the $a/2\langle 011\rangle$ extended dislocation for Cu (in units of $\times 10^2$ GPa).

Material	Char. angle (θ)	K_{11}	K_{22}	K_{12}
Cu	0°	-0.441	-0.441	-0.239
	6.58°	-0.423	-0.468	-0.251
	8.94°	-0.418	-0.478	-0.261
	13.9°	-0.411	-0.501	-0.288
	23.4°	-0.408	-0.544	-0.356
	30°	-0.407	-0.572	-0.407
	36.58°	-0.407	-0.595	-0.458
	46.09°	-0.411	-0.624	-0.534
	60°	-0.442	-0.644	-0.644
	73.9°	-0.501	-0.624	-0.714
	83°	-0.545	-0.595	-0.733
	90°	-0.571	-0.571	-0.736

$$E_{TOT}(\xi_{TP}, \xi_{LP}, s_1, s_2) = E_{STRAIN}(\xi_{TP}, \xi_{LP}, s_1, s_2) + E_{MISFIT}(\xi_{TP}, \xi_{LP}, s_1, s_2) \tag{5}$$

Calculation of the individual energy components is given in the following sections.

2.2.1. *Elastic strain-energy: Anisotropic formalism*

The elastic strain energy $E_{STRAIN}(\xi_{TP}, \xi_{LP}, s_1, s_2)$ of the extended dislocation is obtained by utilizing the anisotropic Eshelby-Stroh (E-S) formalism [30,31]. Three anisotropic interaction coefficients K_{11}, K_{22}, and K_{12} representing the self-interaction of the leading partial, self-interaction of the trailing partial, and the interaction between the two partials, respectively, are tabulated for different dislocation characters and materials on a case-by case basis. Accurate calculation of the strain energy of the extended dislocation necessitates that the coefficients be determined directly from the strain fields calculated based on the anisotropic E-S formalism. The procedure to calculate anisotropic interaction coefficients is elaborated in Appendix A. The obtained anisotropic interaction coefficients for Ni, FeNiCoCrMn, and Cu are provided in Tables 1-3 and the employed anisotropic elastic constants (C_{11} C_{12}, and C_{44}) for the considered materials are given in Table 4. Additionally, in Appendix B, comparison of the current method and the Stroh method for elastic interaction coefficient calculation is provided in detail to emphasize the necessity of employing the present method in this study.

Table 4

Material constants for FCC metals used in this study: intrinsic γ_{isf}; unstable γ_{us} fault energies; lattice constant a, anisotropic elastic constants C_{11}, C_{12}, and C_{44} [32–41].

Materials	a [Å]	C_{11} [GPa]	C_{12} [GPa]	C_{44} [GPa]	γ_{us} [mJ/m^2]	γ_{isf} [mJ/m^2]
Ni	3.52	261	151	132	292	134
Cu	3.61	171.2	123.8	75.6	180	41
Au	4.08	201	170	46	134	33
Al	4.05	114	62	32	162	130
Ag	4.09	131.5	97.3	51.1	133	18
Pb	4.95	55.5	45.4	19.4	87	49
Pd	3.89	234.1	176.1	71.2	287	168
Pt	3.92	357	253	78	339	324
$Ni_{97}Co_3$	3.5224	251.9	152.7	124.4	303	129
$Ni_{90}Co_{10}$	3.5215	251.7	153.1	126.1	285	112
$Ni_{80}Co_{20}$	3.52	251.3	153.7	128.9	270	92
$Ni_{33}Co_{67}$	3.52	238.7	155.3	131.5	205	20
$Ni_{90}Ti_{10}$	3.52	261	151	132	220	126
$Ni_{80}Ti_{20}$	3.52	261	151	132	140	112
FeNiCrCoMn	3.6	221	152	165	439	8
$Fe_{96}N_4$	3.57	487	251	118	510	~0

Consequently, the total continuum strain energy $E_{STRAIN}(\xi_{TP}, \xi_{LP}, s_1, s_2)$ for the extended dislocation can be determined by using the computed anisotropic interaction coefficients. The total strain energy involves the self-interaction energies of the leading and trailing partials ($E^{11}_{elastic}$and $E^{22}_{elastic}$, respectively) and the interaction energy between the two partials ($E^{12}_{elastic}$). Thus, it is expressed as,

$$E_{STRAIN}(\xi_{TP}, \xi_{TP}, s_1, s_2) = E^{11}_{elastic} + E^{22}_{elastic} + E^{12}_{elastic} \tag{6}$$

where the terms on the RHS represent the elastic interaction energy between infinitesimal fractional dislocations belonging to the cores of the partials and they are calculated as:

$$\begin{aligned}
E^{11}_{elastic} &= \int_{-\infty}^{\infty}\int_{-\infty}^{\infty} (K_{11}/2\pi)\rho_{TP}(x)\rho_{TP}(y)\ln|x-y|\mathrm{d}x\mathrm{d}y \\
E^{22}_{elastic} &= \int_{-\infty}^{\infty}\int_{-\infty}^{\infty} (K_{22}/2\pi)\rho_{LP}(x)\rho_{LP}(y)\ln|x-y|\mathrm{d}x\mathrm{d}y \\
E^{12}_{elastic} &= \int_{-\infty}^{\infty}\int_{-\infty}^{\infty} (K_{12}/2\pi)\rho_{TP}(x)\rho_{LP}(y)(\widehat{b}_{TP}.\widehat{b}_{LP})\ln|x-y|\mathrm{d}x\mathrm{d}y
\end{aligned} \tag{7}$$

2.2.2. *Misfit energy: W-S cell model*

The misfit energy $E_{MISFIT}(\xi_{TP}, \xi_{LP}, s_1, s_2)$ of the extended dislocation associated with the disregistry functions $f_{TP,LP}(x_1)$ Eqs. (3,4) is calculated employing a recently proposed novel Wigner-Seitz Cell Misfit (WS-M) model that accounts for the crystal structure and the Wigner-Seitz cell domain area at each atomic-site on the slip plane across which disregistry prevails [28]. This model accurately establishes the varying relative orientations of the crystal structure on the slip plane depending upon the character of the dislocation. The procedure involves a two-dimensional summation of the fault energies on the slip-plane. The fault energies $\gamma(u)$ are sampled from the GSFE landscape of the slip system corresponding to the atomic-sites for the selected character. The rigid shear u corresponding to a specific lattice position is determined from the disregistry functions of the extended dislocation. The GSFE curve precisely quantifies the corresponding energy cost of such shear.

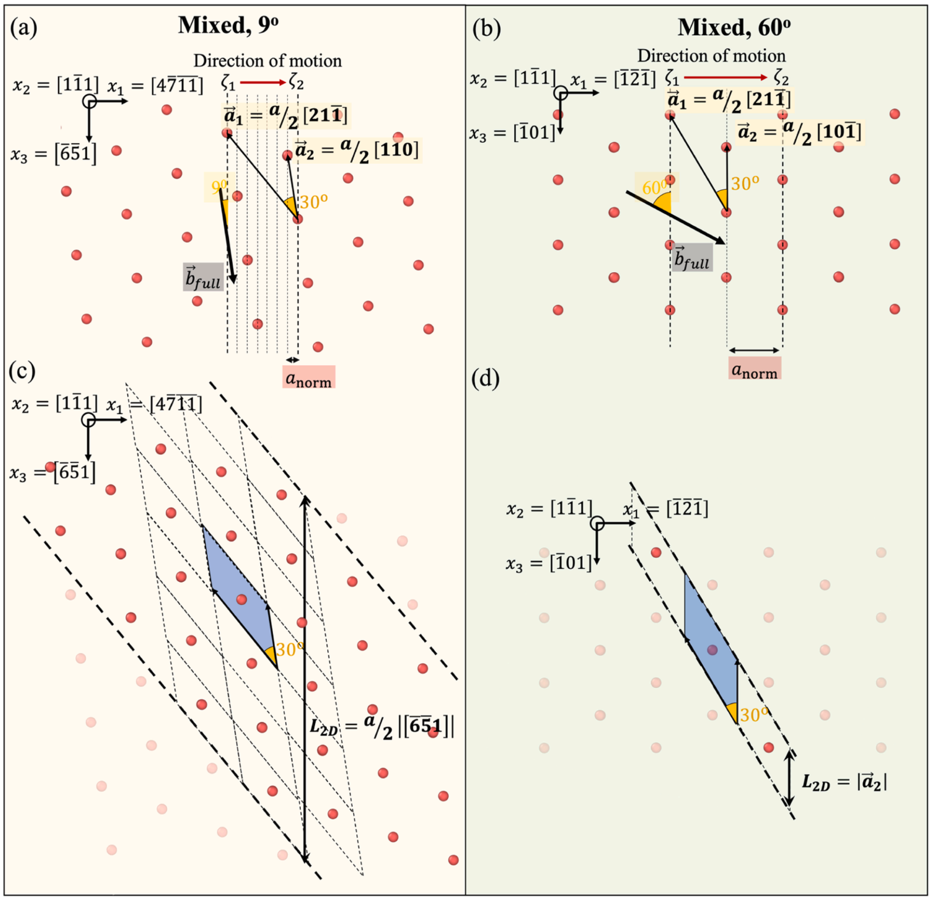

Fig. 2. The lattice structure of the {111} slip plane, for 9° and 60° character of the $a/2\langle 011\rangle$ extended dislocation: (a) the lattice vectors $\vec{a}_1$, $\vec{a}_2$ and respective coordinate system are shown for the 9° mixed dislocation. The dislocation line is parallel to the x_3 direction and direction of motion is along x_1. Two equivalent configurations for the dislocation along the direction of motion are shown by ζ_1 and ζ_2. (b) the lattice vectors $\vec{a}_1$, $\vec{a}_2$ and respective coordinate system are shown for the 60° mixed dislocation. The dislocation line is parallel to the x_3 direction and direction of motion is along x_1. Two equivalent configurations for the dislocation along the direction of motion are shown by ζ_1 and ζ_2. (c) The misfit energy summation is performed along the band bounded by the dashed lines at each Wigner-Seitz Cell area shown by the shaded region. 9°-case slip-plane lattice structure can be reproduced by periodic repetition of the emphasized atomic-sites within a band of length $L_{2D} = a/2|[\bar{6}\bar{5}1]|$ along the dislocation line. (d) The misfit energy summation is performed along the band bounded by the dashed lines at each W-S area shown by the shaded cell. 60°-case slip-plane lattice structure can be reproduced by periodic repetition of the emphasized atomic-sites within a band of length $L_{2D} = \left|\vec{a}_2\right|$ along the dislocation line.

The GSFE curve can be obtained by employing first-principles methods such as Density Functional Theory (DFT) or by using other atomistic simulations including Molecular Statics (MS). For more detailed coverage of the GSFE curve and its derivation, the reader is referred to [22,32].

The GSFE curve of FCC materials is dictated by two critical points, the unstable stacking fault energy barrier, γ_{us}, and the stable intrinsic stacking fault energy barrier, γ_{isf}, and they are provided in Table 4 for the materials considered in this study. With the commonly used sinusoidal restoring-force assumption, the GSFE curve is described by the following function:

$$\gamma(u) \quad = \quad \begin{cases} \dfrac{\gamma_{\text{us}}}{2}\left(1-\cos\left(\dfrac{2\pi u}{b_P}\right)\right), \text{for } 0 \le u \le \dfrac{b_P}{2} \text{ or } \dfrac{3b_P}{2} \le u \le 2b_P \\ \gamma_{\text{isf}} + \left(\dfrac{\gamma_{\text{us}}-\gamma_{\text{isf}}}{2}\right)\left(1-\cos\left(\dfrac{2\pi u}{b_P}\right)\right), \text{for } \dfrac{b_P}{2} \le u \le \dfrac{3b_P}{2} \end{cases} \tag{8}$$

It is more convenient to partition the full GSFE curve for the two Shockley partials as they have distinct Burgers vectors along different <121>-family directions allowing a precise determination of the associated energy cost for each partial. Thus, it is expressed for the trailing and leading partials respectively as:

$$\gamma_{TP}(u) = \begin{cases} \dfrac{\gamma_{\text{us}}}{2}\left(1-\cos\left(\dfrac{2\pi u}{b_P}\right)\right), \text{for } 0 \le u \le \dfrac{b_P}{2} \\ \gamma_{\text{isf}} + \left(\dfrac{\gamma_{\text{us}}-\gamma_{\text{isf}}}{2}\right)\left(1-\cos\left(\dfrac{2\pi u}{b_P}\right)\right), \text{for } \dfrac{b_P}{2} \le u \le b_P \end{cases} \tag{9}$$

$$\gamma_{LP}(u) = \begin{cases} \gamma_{\text{isf}} + \left(\dfrac{\gamma_{\text{us}}-\gamma_{\text{isf}}}{2}\right)\left(1-\cos\left(\dfrac{2\pi u}{b_P}\right)\right), \text{for } 0 \le u \le \dfrac{b_P}{2} \\ \dfrac{\gamma_{\text{us}}}{2}\left(1-\cos\left(\dfrac{2\pi u}{b_P}\right)\right), \text{for } \dfrac{b_P}{2} \le u \le b_P \end{cases} \tag{10}$$

After defining the individual energy curves for the Shockley partials, the next step is calculating the misfit energy for an extended dislocation comprising two distinct Burgers vectors with a total dislocation line length of L. As briefly mentioned, this is fulfilled by finding the corresponding energy cost of the rigid shear introduced by the disregistry function and performing a spatial summation over the discrete lattice sites on the slip plane. The energy cost of such shear is sampled from the GSFE curve using the Eq. (8). The details of this calculation employing the WS-M model are described next.

The WS-M model designates two crystallographic lattice-vectors $\vec{a}_1$ and $\vec{a}_2$ on the slip plane such that the relation $\vec{x}^{(m,n)} = m\vec{a}_1 + n\vec{a}_2$, for integers $m, n \in \mathbb{Z}$, describes all the atomic sites on the slip plane. These two lattice-vectors depend on the crystal structure and the crystallography of the slip-plane as illustrated in Figs. 2 (a, b) for the FCC structure on the {111} slip-plane. A primitive-cell on the slip plane is designated by these two lattice-vectors as shown by the shaded regions in Figs. 2 (c, d). Thus, the total misfit-energy of the dislocation described by the disregistry function f, is calculated as,

$$E_{MISFIT}^{\text{WS-M}} = \sum_{m=-\infty}^{\infty}\sum_{n=-\infty}^{\infty} \gamma\left(f\left(m\vec{a}_1 + n\vec{a}_2\right)\right)(\Delta\text{A}) \tag{11}$$

where ΔA is the area of the W-S cell around each atomic site at position $\vec{x}^{(m,n)} = m\vec{a}_1 + n\vec{a}_2$, γ is given by Eq. (8) and f by Eq. (1). Note that

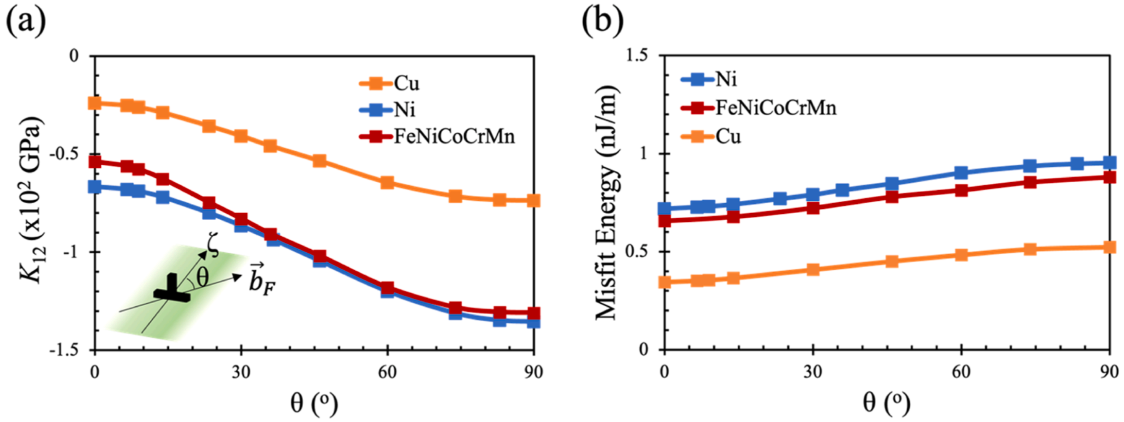

Fig. 3. (a) Anisotropic interaction coefficient K_{12} is plotted for Cu, Ni, and FeNiCoCrMn vs. dislocation character suggesting a stronger elastic repulsion between the partials for the edge character; (b) Misfit energy vs. dislocation character is plotted for Ni, FeNiCoCrMn, and Cu indicating a monotonic trend for the spectrum between the screw and edge characters.

depending on the character of the extended dislocation, the orientation of the lattice with respect to the global $x_1 - x_2 - x_3$ axes varies as demonstrated in Figs. 2 (a, b) for 9° and 60° dislocations. Thus, the relative atomic sites also change depending upon the character of the dislocation. The direction of motion for the dislocation is shown in Figs. 2 (a, b), and two equivalent positions are shown by ζ_1 and ζ_2. As the dislocation moves, it passes through the dashed lines and reaches the subsequent equivalent position (refer Figs. 2 (a, b)). The interplanar spacing along the direction of motion is shown by a_{norm} on the $(1\bar{1}1)$ slip-plane for the two example cases. Note that, a_{norm} differs significantly with character, which has critical implications on the CRSS and will be elaborated further in the following sections.

The misfit energy expression can be further simplified by exploiting the high symmetry of the slip plane without a loss of generalization. In fact, it is sufficient to perform the spatial summation over the atomic-sites within the bands with a spacing of L_{2D} shown in Figs. 2 (c, d) as these bands repeat periodically along the dislocation line. L_{2D} is half periodicity along dislocation line direction, x_3, and determined by $L_{2D} = a/2|\langle lmn\rangle|$, where $\langle lmn\rangle$ is the crystallographic direction along x_3. Thus, utilizing this symmetry the misfit energy expression simplifies to,

$$E_{MISFIT}(\xi_{TP}, \xi_{TP}, s_1, s_2) = \frac{1}{L_{2D}} \sum_{m=-\infty}^{\infty} \sum_{n=-N_0}^{N_1} \gamma\left(f\left(m\vec{a}_1 + n\vec{a}_2\right)\right)(\Delta A) \tag{12}$$

where $(L_{2D}, N_0, N_1) = (a/2|[\bar{6}51]|, 3, 4)$ for the case of $a/2\langle 011\rangle$ 9° dislocation, and $(L_{2D}, N_0, N_1) = (|\vec{a}_2|, 0, 0)$ for the 60° dislocation case, γ is given by Eq. (8) and f by Eq. (1). The energy is normalized by the length L_{2D} so that the misfit-energy measure is normalized per unit length of the dislocation line.

Rewriting the total misfit energy expression with the partitioned fault-energies (given by Eqs. (9) and (10)) for the individual Shockley partials (described by Eqs. (3) and (4)) as,

$$E_{MISFIT}(\xi_{TP}, \xi_{TP}, s_1, s_2) = \frac{1}{L_{2D}} \left[\begin{array}{l} \sum\limits_{n=-N_0}^{N_1} \sum\limits_{m=-M_{\max}}^{-1} \gamma_{TP}\left(f_{TP}\left(x_1^{(m,n)}\right)\right)(\Delta A) \\ \ldots + \sum\limits_{n=-N_0}^{N_1} \sum\limits_{m=0}^{M_{\max}} \gamma_{LP}\left(f_{LP}\left(x_1^{(m,n)}\right)\right)(\Delta A) \end{array} \right] \tag{13}$$

where $x_1^{(m,n)} = (m\vec{a}_1 + n\vec{a}_2).\hat{e}_1$. A large summation limit of $M_{\max}$ is chosen, in the order of 10^4, so that computed misfit energy $E_{MISFIT}(\xi_{TP}, \xi_{LP}, s_1, s_2)$ is sufficiently converged. The misfit-energy given by Eq. (13) is calculated per unit length of the dislocation line. Consequently, the misfit-energy of the extended dislocation can be calculated as a function of four parameters $(\xi_{TP}, \xi_{LP}, s_1, s_2)$ using the Eq. (13).

2.3. *Determination of core-structure parameters*

Having computed the continuum elastic energy $E_{STRAIN}(\xi_{TP}, \xi_{LP}, s_1, s_2)$ and the atomistic misfit energy $E_{MISFIT}(\xi_{TP}, \xi_{LP}, s_1, s_2)$ as a function of the dislocation core widths (ξ_{TP}, ξ_{LP}) and the positions of the partials (s_1, s_2), one can now determine the total energy of the extended dislocation $E_{TOT}(\xi_{TP}, \xi_{LP}, s_1, s_2)$ from the Eq. (5). The core-parameters of the extended dislocation $(\xi_{TP}^0, \xi_{LP}^0, s_1^0, s_2^0)$ that minimizes the total energy E_{TOT} are determined by solving the equations:

$$\frac{\partial E_{TOT}}{\partial \xi_{TP}} = 0; \frac{\partial E_{TOT}}{\partial \xi_{LP}} = 0; \frac{\partial E_{TOT}}{\partial s_1} = 0; \frac{\partial E_{TOT}}{\partial s_2} = 0 \tag{14}$$

For more detailed coverage of how each energy component changes with the core-parameters readers are referred to the authors' previous study [28]. The minimizing parameters $(\xi_{TP}^0, \xi_{LP}^0, s_1^0, s_2^0)$ are then used to determine the CRSS as described in the following sections.

2.4. *Effect of dislocation character on energy constituents*

The character of the dislocation influences its CRSS through modifications on the two main aspects. First, the strain energy varies with dislocation character, which is reflected in the computed anisotropic interaction coefficients. Second, the misfit-energy changes significantly with the character of the dislocation. The effect of these individual energy terms is discussed next.

2.4.1. *Effect of mixed character on strain energy*

The anisotropic interaction coefficients for the two partials are shown in Fig. 3 (a) for the entire range between the edge and screw dislocations. K_{12} being negative implies that the interaction between the partials is repulsive so the strain energy decreases as the separation of the partials increases. The trend is similar for the three materials shown in the figure. In all cases, the edge character has the lowest interaction coefficient meaning that the repulsive force between the partials is the highest in that case. Note that, K_{12} lies in a similar range for Ni and FeNiCoCrMn, and, in fact, they almost overlap in a certain range covering the mixed character. This is a combined outcome of the elastic constants and the effect of dislocation character on the computed strain fields.

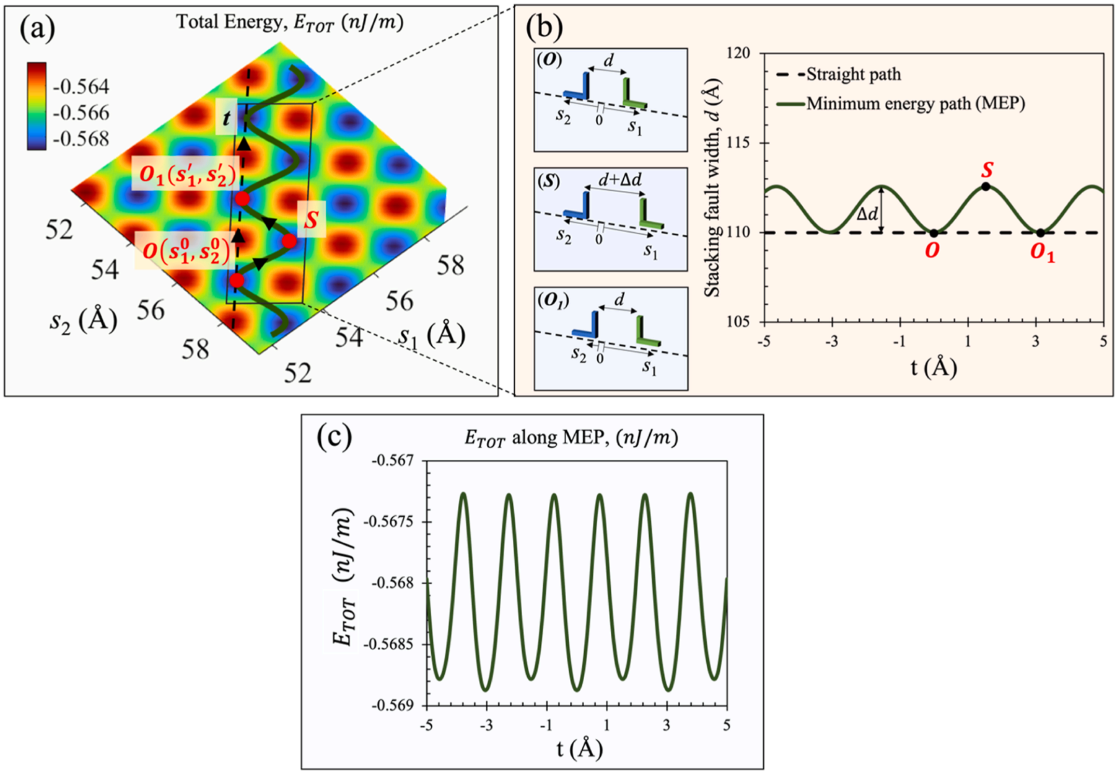

Fig. 4. Total-energy landscape of the $a/2\langle 011\rangle$ extended dislocation for a screw-dislocation in FeNiCoCrMn (a) Plot of total-energy E_{TOT} against the position of the Shockley partials (s_1, s_2) indicating possible paths traversing across the energy minima $O = (s_1^0, s_2^0)$, $O_1 = (s_1', s_2')$; the dashed-line represents a straight-path in which the partials move together such that stacking-fault width between them is conserved i.e. $s_1 + s_2 = C$, is constant; the solid-line represents a zig-zag Minimum-Energy Path (MEP) where the partials move intermittently, passing through an intermediate transition state S (b) Schematic representation of the motion of the partials along the MEP, in which the leading partial moves first, increases the fault-width from d to $d + \Delta d$ and then the trailing partial follows; a plot of the variation of the stacking-fault width during the motion is given (c) Plot of the total energy variation along the MEP.

2.4.2. *Effect of mixed character on misfit energy*

Misfit-energy shows a monotonic trend with the character as plotted in Fig. 3 (b) for the three materials. It is controlled by the critical points on the GSFE curve together with the core-widths of the partials and the stacking fault width. The misfit-energy is mainly dominated by the stacking fault width and a similar trend can be seen in the stacking fault-width vs. character plot as will be given in the following sections. Further, the edge character has the highest misfit energy of all three materials. This is due to two main reasons: (*i*) it implies a much wider core (*ii*) the stacking fault width is the highest for the edge compared to other characters.

2.5. *CRSS of $a/2\langle 011\rangle$ extended dislocation*

The Peierls-Nabarro (P-N) framework is the standard method employed to determine the CRSS [42]. However, this method cannot be directly applied in the present case due to several critical aspects: (*i*) it doesn't account for the motion of the individual Shockley partials and only considers the full dislocation, (*ii*) the contribution from the elastic strain energy is ignored and only the misfit-energy is considered, (*iii*) effect of character cannot be correctly captured because the actual atomic-sites are not involved in the calculation. Thus, in this study, we utilize the recently proposed method to calculate the CRSS that is faithful to the crystal structure and considers the individual motion of the partials contributing to the overall CRSS, as established in detail in the authors' previous study and briefly described here for the readers' convenience [28]. One of the main challenges in the field for CRSS calculation has been the accurate calculation of the dislocation core-width. The glide stress of a dislocation is highly sensitive to the employed core-width value. Thus, there has been numerous attempts to address this by proposing different approaches for core-width determination [6,43–45]. The precise calculation of core-width requires that the total energy of the dislocation is minimized to give the equilibrium core structure of the dislocation. Thus, the elastic and misfit energies need to be precisely captured for the total energy minimization to yield the correct core-width of the dislocation.

The total energy, E_{TOT}, against the position of the Shockley partials (s_1, s_2) is plotted in Fig. 4 for the screw character $a/2\langle 011\rangle$ extended dislocation in FeNiCoCrMn. The energy surface has multiple energetically-degenerate minima as illustrated in Fig. 4 by points $O = (s_1^0, s_2^0)$, $O_1 = (s_1', s_2')$. These minima represent energetically equivalent configurations for an extended dislocation on the slip plane. Note that S is not an equivalent configuration as it implies a different stacking fault width $(s_1 + s_2)$ compared to the points $O = (s_1^0, s_2^0)$ and $O_1 = (s_1', s_2')$. However, in the case of very low stacking fault energy materials e.g. FeNiCoCrMn, these points have very similar energy values as a small increase or decrease in the stacking fault width does not alter the total energy as much compared to high stacking fault energy materials. Subsequently, to calculate the CRSS, the pathway containing these minima must be determined so that the energy-trajectory corresponding to the specific path representing the motion of $a/2\langle 011\rangle$ extended dislocation can be drawn from the landscape. Finally, the CRSS of the extended dislocation is determined from the maximum gradient on the energy-trajectory of the obtained pathway by considering the individual motion of each partial.

For the $a/2\langle 011\rangle$ extended dislocation in FeNiCoCrMn the energy-trajectory is shown in Fig. 4 (a) by the solid line which passes through O, S, and O_1, in the given order. The energy-trajectory represents the

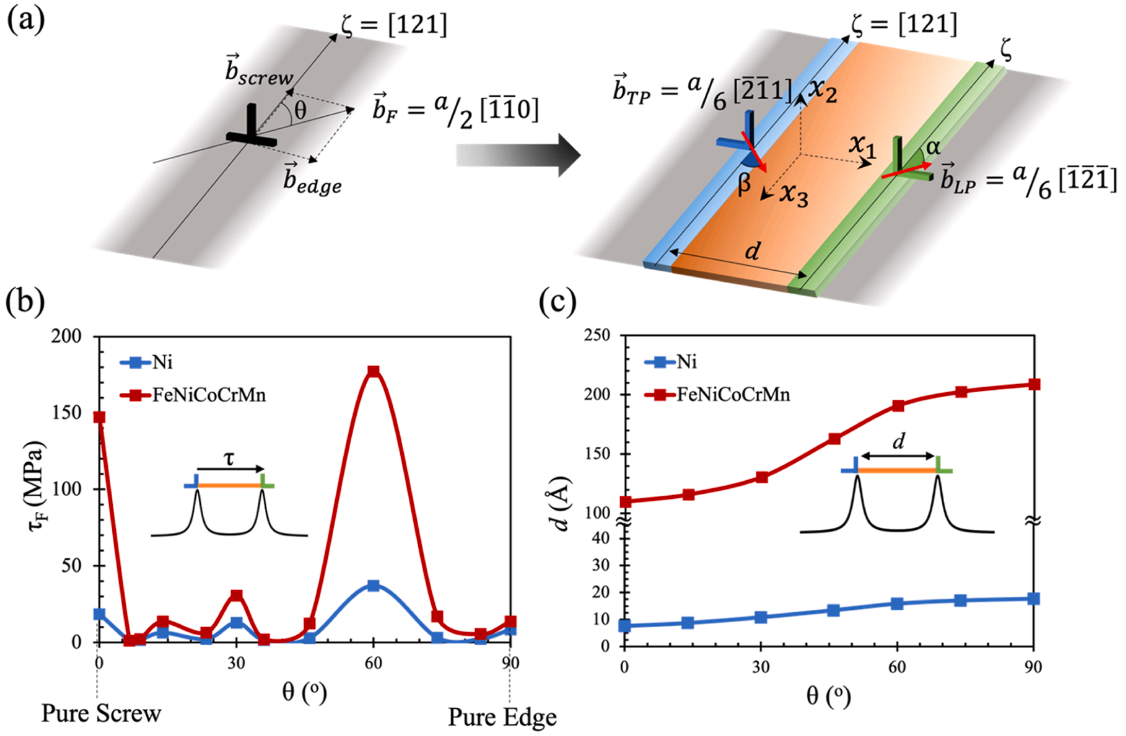

Fig. 5. Effect of dislocation character on CRSS, core-width and stacking fault width (a) A schematic of the $a/2[\bar{1}\bar{1}0]$ extended dislocation, its edge/screw components and its Shockley partials; the angles θ, α, and β are defined indicating the mixed nature of the full dislocation and the individual partials respectively (b) Variation of CRSS of the extended dislocation against θ (c) Variation of stacking fault width of the extended dislocation against θ.

motion of individual Shockley partials as their positions (s_1, s_2) vary from one energetically-degenerate position, O, to the next one, O_1. Thus, these variations in the positions of individual Shockley partials (s_1, s_2) dictate the path taken by the $a/2\langle 011\rangle$ extended dislocation. The energy trajectory is determined by utilizing the "Minimum-Energy Path" (MEP) which implies the least resistance for the motion of the $a/2\langle 011\rangle$ extended dislocation. To describe this periodic path we utilize a Fourier-series based approach that is expressed by the following equations,

$$s_1(t) = s_1^0 + \left(\frac{1}{\sqrt{2}}\right)\left(t + C_0 + \sum_{k=1}^{n} C_k\left(1 - \cos\frac{2\pi t}{C_P}\right)\right)$$
$$s_2(t) = s_2^0 + \left(\frac{1}{\sqrt{2}}\right)\left(-t + C_0 + \sum_{k=1}^{n} C_k\left(1 - \cos\frac{2\pi t}{C_P}\right)\right) \tag{15}$$

where the maximum number of periodic functions is set to be $n = 4$, sufficient to reach the desired level of accuracy. t is the parametrization variable so that the positions of the partials are given by $(s_1(t), s_2(t))$ with O being the origin and $(C_0, C_1, C_2, C_3, C_4, C_P)$ is a set of parameters that defines the path which connects the energetically degenerate positions (e.g. O and O_1) implying equivalent configurations for the extended dislocation on the total energy landscape. The origin O is a minimum point that represents a stable configuration for the extended dislocation at which $t = 0$, $s_1^0 = s_1(0)$ and $s_2^0 = s_2(0)$. Note that, the straight-path connecting O and O_1 is modeled by setting the parameter values $C_0 = C_1 = C_2 = C_3 = C_4 = 0$, and for any $C_P \neq 0$ as illustrated by the dashed line in Fig. 4 (a). Nevertheless, for any other set containing non-zero parameter values the path is not straight but zig-zag in nature as shown by the solid-line in Fig. 4 (a). The energy trajectory of the path is calculated at discretized points by letting $t_i = i\Delta t$, where $\Delta t = 0.01\text{Å}$. Finally, the total cumulative energy of the path is computed by the objective function expressed as:

$$E_{PATH}(C_0, C_1 \ldots, C_P) = \sum_{i=1}^{T_{\max}} E_{TOT}\left(s_1(t_i), s_2(t_i), \xi_{TP}^0, \xi_{LP}^0\right) \tag{16}$$

A large enough upper limit, 2000, is chosen for the summation that is sufficient to capture the periodicity of the MEP. The set of parameters $(C_0, C_1, C_2, C_3, C_4, C_P)$ defining the Minimum Energy Path (MEP) is determined by the minimization of the total cumulative energy of the path, E_{PATH}, using MATLAB®. As shown by the solid line in Fig. 4 (a), the MEP is not straight but involves a zig-zag pattern avoiding the higher energy peaks to achieve the least resistance to glide. Additionally, as the extended dislocation moves tracing this path the stacking fault width, given by $d(t) = s_1(t) + s_2(t)$, fluctuates as shown in Fig. 4 (b). The amplitude of this fluctuation, given by Δd, is specific to the case and controlled by properties such as elastic constants, fault energy barrier, and dislocation character.

Finally, the CRSS of the extended dislocation is determined utilizing the Optimum-Energy-Trajectory (OET) approach for CRSS prediction for FCC materials. This approach enables accurate calculation of the CRSS of an extended dislocation by individual treatment of the Shockley partials. For more detailed coverage of the OET approach and its derivation reader is referred to [28]. In the current analysis, uniaxial tensile load is applied in the $\hat{v}\|[1\bar{3}2]$ direction leading to a global stress tensor given by $\underline{\underline{\sigma_a}} = \sigma_a(\hat{v} \otimes \hat{v})$. This direction is chosen so that both leading and trailing partials have the same Schmid factors. Consequently, the CRSS is obtained by resolving the critical applied stress along the slip system of the extended dislocation, which is expressed as,

$$\tau_F = SF_{FULL}\max\left(\frac{1}{SF_{LP}s'_1(t) - SF_{TP}s'_2(t)}\left(\frac{1}{b_F}\frac{dE_{TOT}}{dt}\right)\right) \tag{17}$$

where SF_{LP} and SF_{TP} are the Schmid factors for the leading and trailing partials respectively, and $s_1(t)$, $s_2(t)$ parametrize the MEP. $SF_{FULL} = (\hat{v}.\hat{n}_{slip})(\hat{v}.\hat{b}_F)$ is the Schmid factor for the full extended dislocation on its

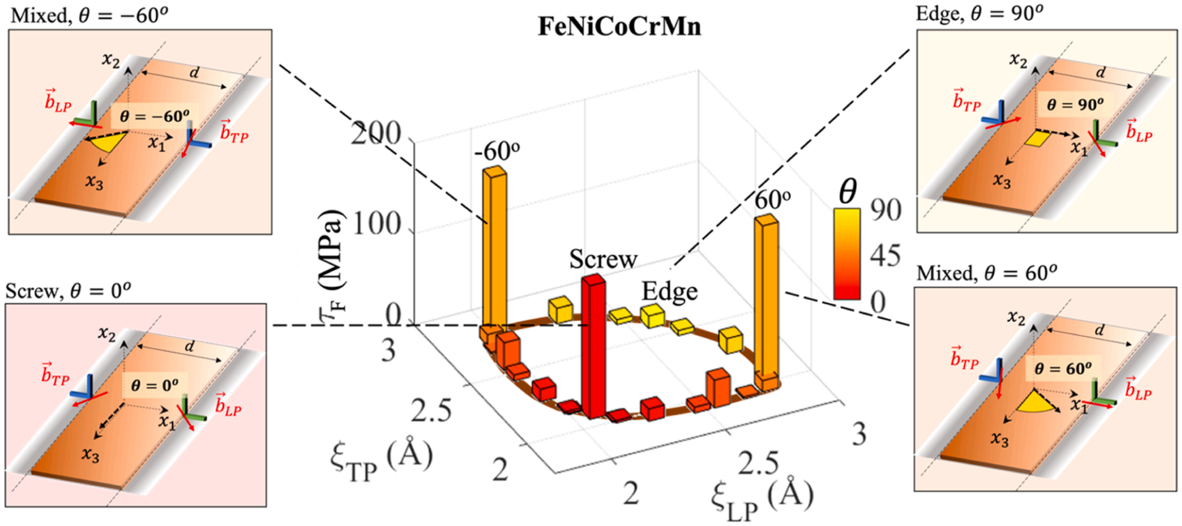

Fig. 6. Core-widths of the leading (ξ_{LP}) and trailing partials (ξ_{TP}) are plotted against the character angle, θ, measured from the color-bar and corresponding CRSS. Four example cases for dissociated dislocation structures schematically shown indicating the Burgers vector directions of the partials and the associated θ angle.

slip system, with $\widehat{b}_F$ representing the unit vector along the direction of the Burgers vector $\vec{b}_F$. The Schmid factors are given by the equations $SF_{LP} = (\widehat{v}.\widehat{n}_{slip})(\widehat{v}.\widehat{b}_{LP})$ and $SF_{TP} = (\widehat{v}.\widehat{n}_{slip})(\widehat{v}.\widehat{b}_{TP})$, where $\widehat{b}_{TP}$ and $\widehat{b}_{LP}$ are unit vectors along the Burgers vectors of the trailing and leading partials respectively, and $\widehat{n}_{slip} = 1/\sqrt{3}[1\bar{1}1]$ is the slip plane normal.

2.6. Effect of character on CRSS

The developed framework can analyze mixed dislocations with arbitrary characters. This is made possible through advancements on two fronts: (a) the use of the Eshelby-Stroh formalism (Section 2.2.1) that is capable of determining the strain-fields, and consequently the strain-energy, of a dislocation with arbitrary character and (b) proposition of calculation of the misfit energy accounting for the correct atomic-sites on the slip plane for the chosen dislocation character. Existing approaches have by and large focused only on special cases of dislocation character, namely of “edge” and “screw” types. The primary reason, in the authors’ opinion, is the simplifications afforded by these assumptions in their respective frameworks, either in determining the strain-field, calculation of misfit energy, and consequently the core-widths. This limits the predictability since dislocations in real materials are curved with varying characters along their length. However, the proposed framework can determine this maximum CRSS by analyzing all characters. The efficacy of the framework in this regard is illustrated by calculating the core-parameters and the CRSS for the $a/2\langle 011\rangle$ dislocation covering the spectrum between “screw” and “edge” characters. The results are presented in Fig. 5. Note that the CRSS exhibits a non-trivial fluctuation between edge and screw natures (refer Fig. 5 (a)). In fact, it exhibits a maximum in the CRSS for the 60°-mixed character of dislocation that would otherwise have been missed if only the screw and edge natures were considered. Available experimental data for FeNiCoCrMn and Ni are in agreement with the results of the present study. For instance, for FeNiCoCrMn our prediction of 178 MPa for the 60° case is within 5% of the experimental value of 172 MPa obtained from experiments done on single crystals [46,47]. Also, experimental measurements for edge dislocations in Ni lie in 4.7-9 MPa which is in close agreement with the current prediction of 8.6 MPa [42,48].

The developed framework employs the average fault energetics of the material. One should note that, in the case of alloys there could be other factors contributing to the CRSS such as local solute distribution and short-range ordering [49–51]. Moreover, the input material properties are taken for 0 K as they can be reliably obtained from DFT simulations. For extension to finite-temperatures, the predicted energy-barriers along with MEP could serve as the activation-energy in an Arrhenius-type expression to predict CRSS at finite temperatures [52,53].

In this study, our focus is on the character effect which is incomplete for mainly two reasons: (a) The Wigner-Seitz cell based integration for misfit-energy is missing and prior treatments that treat the actual lattice as a simple cubic will indeed produce a much higher CRSS. The Wigner-Seitz cell naturally brings a dislocation character dependence that differs from the formulas based on a simple cubic lattice. We highlight the differences in Appendix D. The formulas for character effect in the literature give a smooth variation of the properties contrary to our findings in this paper and also trends given in FCC based alloys [54], (b) the intermittent motion of the partials (one partial moves first followed by the other) depends on the dislocation character and lowers the CRSS levels by avoiding higher energy peaks in the total energy surface as shown in Fig. 4 (a). We note that the intermittent motion (b) also depends on the relative unstable and intrinsic fault energies and is far more significant in the low γ_{isf} cases. Such non-trivial variations are dependent on the balance between the continuum strain-energy and misfit-energy for that character, which is controlled by the elastic anisotropy, underlying fault energies, and respective crystal orientation for the character. The proposed framework is able to model and predict the sensitivity of CRSS with character complementing prior studies [49,55]. Further, it is an experimentally very demanding task to precisely capture these variations, which underscores the importance and practicality of the analytical predictive model. Also, note that the stacking fault width also exhibits dramatic changes of similar nature (Fig. 5 (b)), exhibiting a near doubling of the fault width for Ni and FeNiCoCrMn across the spectrum of characters as consistent with experimental observations [56,57]. Such a thorough analysis of the effect of character is important and necessary to predict the CRSS, and consequently the yield strength of material reliably.

2.6.1. Character-dependent asymmetry of core-widths and its effect on the CRSS

Another complexity of the mixed dislocations is their asymmetric dislocation density distributions on the slip plane as briefly discussed in Section 1 (refer Fig. 1 (c)). This asymmetry is due to the distinct core-

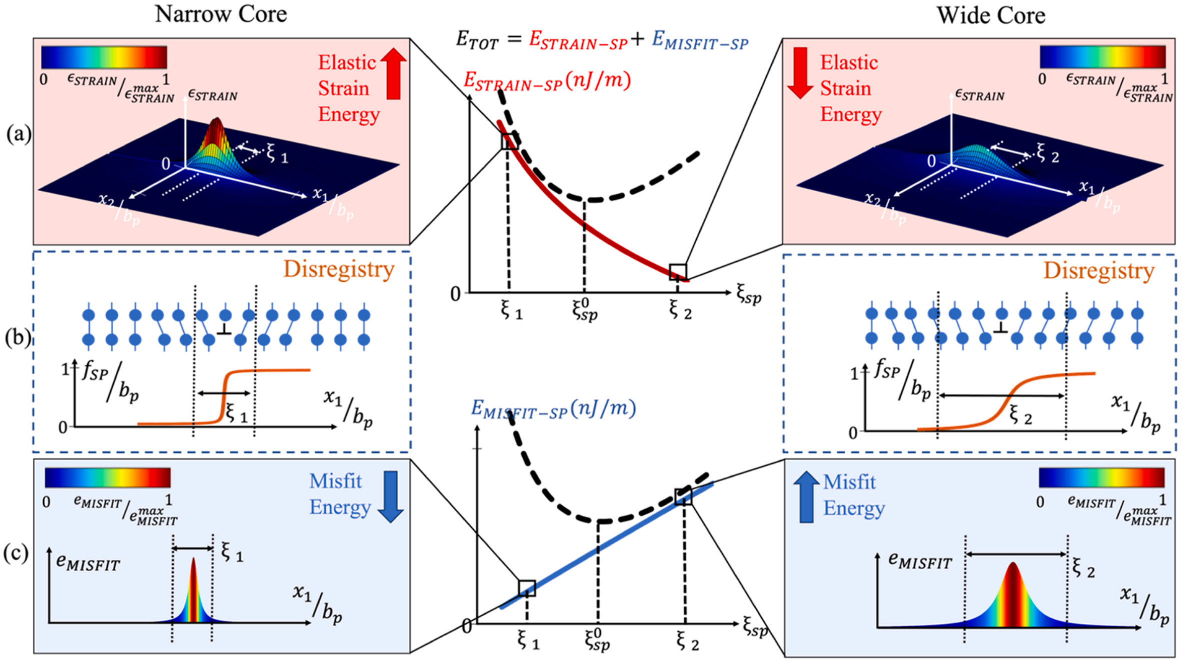

Fig. 7. Variation of continuum strain-energy and atomistic misfit-energy as a function of core-width for an isolated Shockley partial (a) The strain-energy, given by $E_{STRAIN-SP}$, reduces with increasing core-width owing to a more spread-out core; this reduces the repulsive interaction between infinitesimal fractionals within the core leading to lower strain energy (b) Plot of the disregistry distribution f_{SP} at low and high core-widths, presented along with a schematic atomic-structure surrounding the dislocation (c) The misfit energy, given by $E_{MISFIT-SP}$, increases with increasing core-width owing to larger area of misfit on the slip plane; the total energy E_{TOT} given by the sum of the strain-energy and misfit-energy varies as shown by the dashed line exhibiting a clear minimum at the equilibrium core-width ξ_{SP}^0.

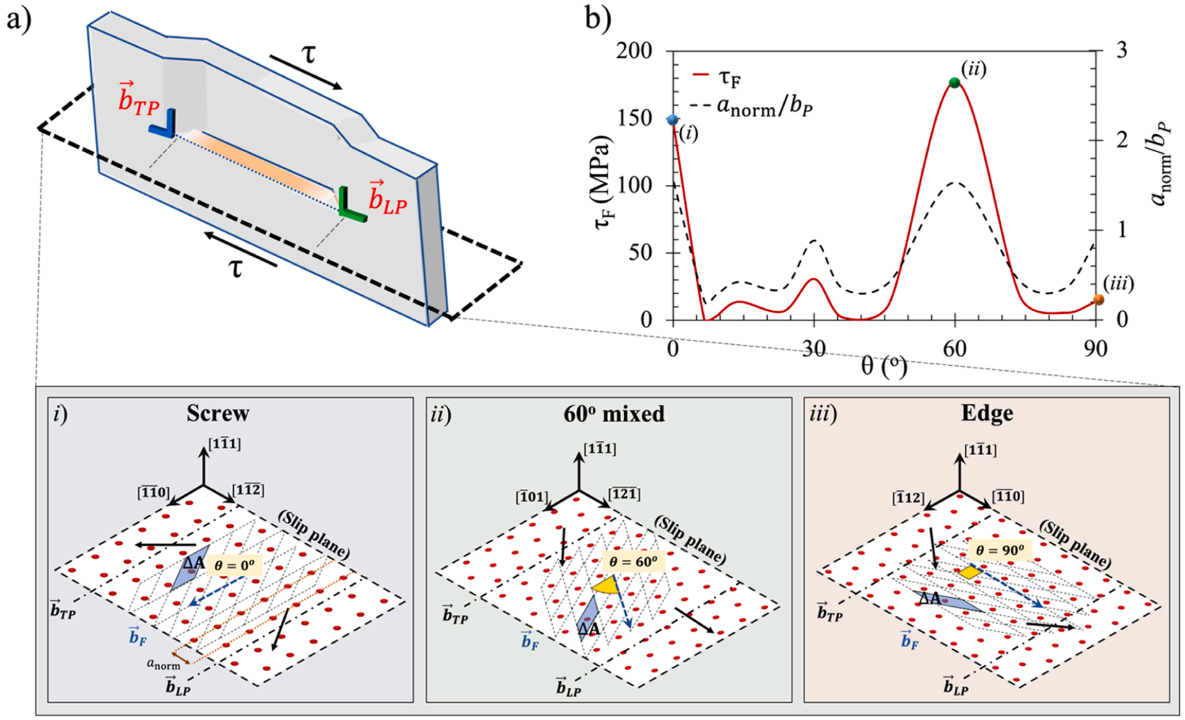

Fig. 8. (a) Atomic arrangements on the slip plane for (*i*) screw, (*ii*) 60-degree, and (*iii*) edge cases. Relative orientations of the Burgers vectors are shown for leading and trailing partials by the black arrows and for full dislocations by the dashed blue arrow. The character of the dislocation is measured by the angle θ as shown for each case. (b) The variation of CRSS and a_{norm} is plotted against the character of the dislocation indicating the correlation between the two parameters.

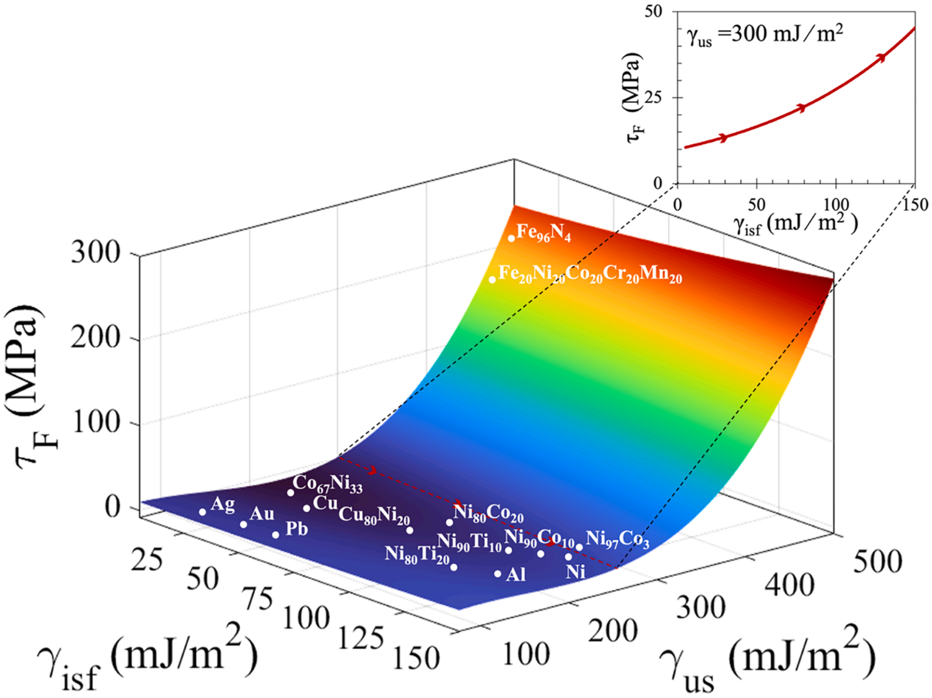

Fig. 9. Dependence of the CRSS of $a/2[\bar{1}\bar{1}0]$ extended dislocation, τ_F, on the fault energy barriers, illustrating a coupled dependence on both the unstable stacking fault energy γ_{us} and intrinsic stacking fault energy γ_{isf}.

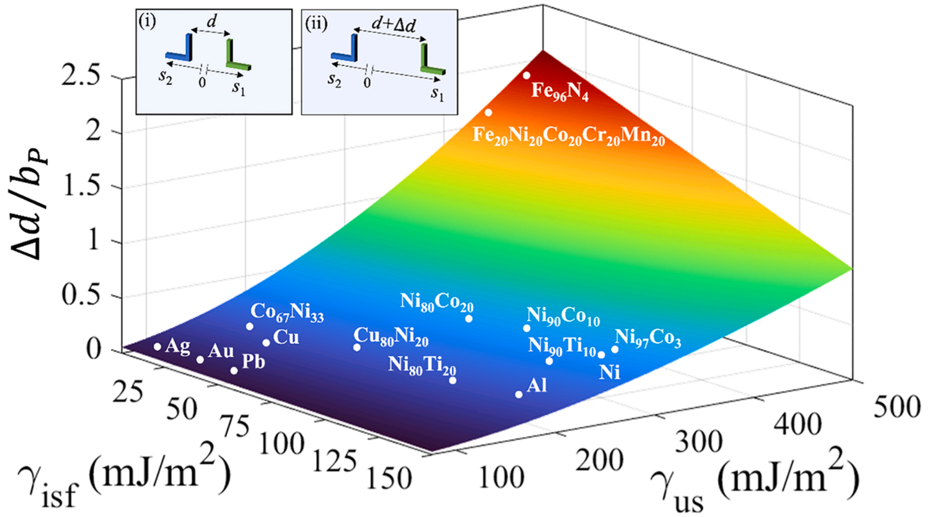

Fig. 10. Dependence of the amplitude of fluctuation $\Delta d/b_P$ in SFW during motion of an extended dislocation on the fault energy barriers, illustrating a coupled dependence on both the unstable stacking fault energy γ_{us} and intrinsic stacking fault energy γ_{isf}. (i), (ii) are schematic representations of the intermittent motion of the partials for an extended dislocation.

widths of the individual partials as plotted for a range of characters in Fig. 6 for FeNiCoCrMn. Each bar in Fig. 6 represents a specific dislocation character, and the corresponding CRSS value is measured from the z-dimension. The x-y axes are showing the equilibrium core-widths of the leading and trailing partials for different dislocation characters, and it has a doughnut-looking shape when plotted for the entire spectrum between the edge and screw dislocations. As mentioned, the partials and the parent full dislocation have distinct characters as the dissociation dictates. This is illustrated for four cases in Fig. 6 where the character of the full dislocation is expressed by θ and Burgers vector directions of the partials are shown by the red arrows. For instance, in the case of 60°-mixed dislocation, the trailing partial is of edge character whereas the leading partial is a 30°-mixed dislocation. On the contrary, for the 60° case it is vice-versa. Further, for the pure edge and screw dislocations, the partials are 30° and 60°-mixed, respectively.

Moreover, this asymmetry of the density distribution dictates the energy path taken by the extended dislocation as the two partials have distinct barriers to glide. For instance, in the case of 60°-mixed dislocation, the trailing partial is of edge character and has a lower barrier for motion since it has a wider spread core that reduces its friction stress. However, the other Shockley partial is a 30°-mixed dislocation, hence it has a smaller core-width and a higher resistance to glide. Thus, the edge

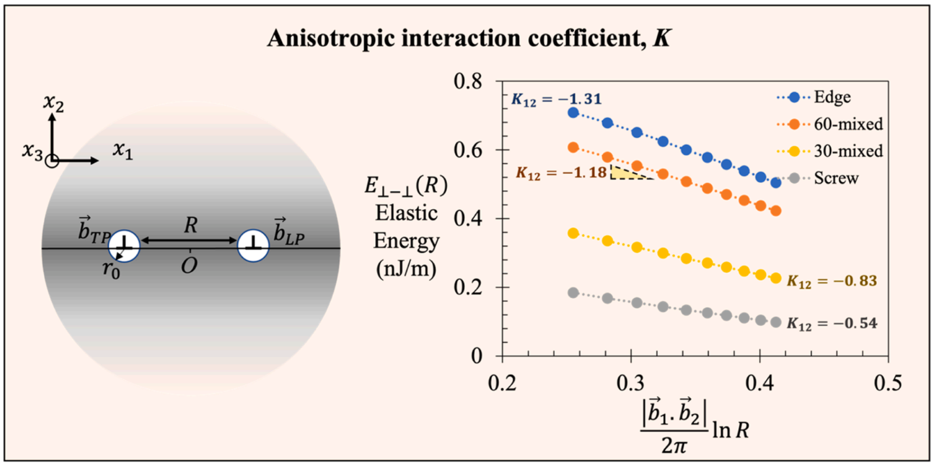

Fig. A.1. Schematic representation of the integration setup to compute the elastic strain-energy of a two-dislocation system in an anisotropic media; the Burgers vectors of the two dislocations are given by $\vec{b}_{TP}$ and $\vec{b}_{LP}$ respectively positioned at $O_2(-R/2, 0)$ and $O_1(R/2, 0)$ respectively. The strain-energy density is numerically integrated to yield the energy of interaction $E_{\perp-\perp}(R)$ as a function of the separation distance R, and the slope of variation of this function yields the anisotropic coefficient K_{12} (corresponding to the interaction between the trailing partial and leading partial).

Table B1
Anisotropic interaction coefficients computed from the current method (K_{11} and K_{12}), and the Stroh method (K^E_{11} and K^E_{12}) in GPa.

Materials	θ	K_{11} [GPa]	K^E_{11} [GPa]	K_{12} [GPa]	K^E_{12} [GPa]
Ni	0°	-93.2	-66.3	-66.6	-4.1
Ni	90°	-110.9	-65.8	-135.3	0
FeNiCoCrMn	0°	-86.2	-65.5	-53.8	-7.4
FeNiCrCoMn	90°	-106.9	-63.7	-130.9	0

Table B2
Prelogarithmic energy factors computed from the current method (G_{11} and G_{12}), and the Stroh method (G^E_{11} and G^E_{12}) in GPa × Å^2.

Materials	θ	G_{11} [GPa × Å^2]	G^E_{11} [GPa × Å^2]	G_{12} [GPa × Å^2]	G^E_{12} [GPa × Å^2]
Ni	0°	-30.6	-15.9	-10.9	-5.1
Ni	90°	-36.4	-19.8	-22.2	-12.6
FeNiCoCrMn	0°	-29.6	-15.3	-9.2	-4.1
FeNiCrCoMn	90°	-36.9	-20.0	-22.6	-12.9

Table B3
Core-widths ($\xi_{TP,LP}$), Stacking fault widths (d), and friction stresses (τ_F) for Ni (screw) using both anisotropic interaction coefficient methods.

Material	Character	K-Method	$\xi_{TP,LP}$ [Å]	SFW [Å]	τ_F [MPa]
Ni	Screw	Stroh method	(3.65, 3.65)	6.8	37.4
Ni	Screw	Current study	(3.52, 3.52)	7.6	18.7

partial is more mobile than the 30° partial creating an asymmetry for the motion of the extended dislocation which is inherently incorporated within the proposed framework. This complex interplay between the partials and their interaction controls the total energy landscape of the extended dislocation, which is then used to predict the CRSS by finding the corresponding MEP for the specific case. This complexity precludes devising a simple empirical relationship between the CRSS and character and entails that the CRSS be calculated on a case-by-case basis employing the proposed framework.

3. Discussion

The present study establishes a predictive analytical framework for the CRSS of $a/2\langle 011\rangle$ extended dislocation with an arbitrary character in FCC materials While the model can be extended to other crystal structures, there are certain complexities that must be considered. For instance, in HCP crystals W-S cell area would differ depending on basal, prismatic, and pyramidal systems. Additionally, the distinction between the dense and loose planes, and highly distorted GSFE profiles deviating from simple sinusoidal description need to be addressed [58–61]. Further, in BCC crystals the dislocation core is spread on multiple planes

Table C1
Calculated and measured Stacking fault widths (d), core-widths ($\xi_{TP,LP}$), and friction stresses (τ_F) in pure Al.

Pure Al	Method	Character	d, Å	$\xi_{TP,LP}$, Å	τ_F, MPa
This study	PN based	0°	0 (undis.)	(2.8, 2.8)	87.8
		60°	6.05	(3.9, 2.8)	58.3
		90°	7.65	(3.5, 3.5)	13.9
Experiments	TEM Studies	0°	0 [a], [a*](undis.)		
		60°	5.5[b]		
		90°	8.0[c]		
Bulatov *et al.* (DFT) [65]	PN based	0°		(2.1, 2.1)	256.4
		60°		(3.0, 2.9)	97.7
		90°		(3.5, 3.2)	3.2
Bulatov *et al.* (EAM) [65]	PN based	0°		(3.7, 3.4)	88.1
		60°		(5.4, 5.7)	44.9
		90°		(6.4, 5.2)	24.0
	PN based	0°	0 (undis.)		
Schoeck [75]		90°	7.4		
Carter *et al.* [76]	OFDFT	0°	0 (undis.)		355
		90°	20.4		1.6
Beyerlein *et al.* [77]	PFDD	0°	2.6		77.8
		90°	6.3		19.7
Woodward *et al.* [78]	DFT	0°	5.0		
		90°	7.0		
Olmsted *et al.* [64]	EAM	0°			16
		60°			21
		90°			2

[a] – experiment [79]
[a*] - experiment, private communication with T. Waitz, University of Vienna [80]
[b] – experiment [81]
[c] – experiment [79]
undis. – undissociated

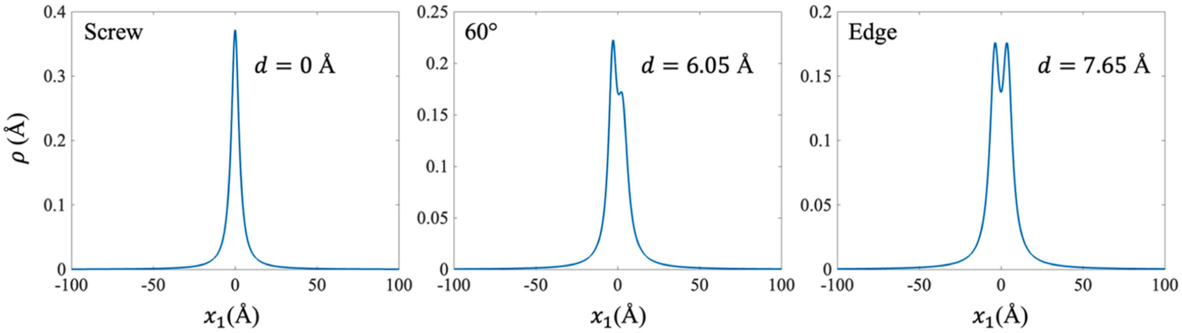

Fig. C1. Dislocation density distributions for screw, 60°, and edge cases for pure Al. Note the asymmetry of the core widths for the 60° case and the symmetry of the core widths for the edge case. Also, note the prediction of an undissociated dislocation for the screw case.

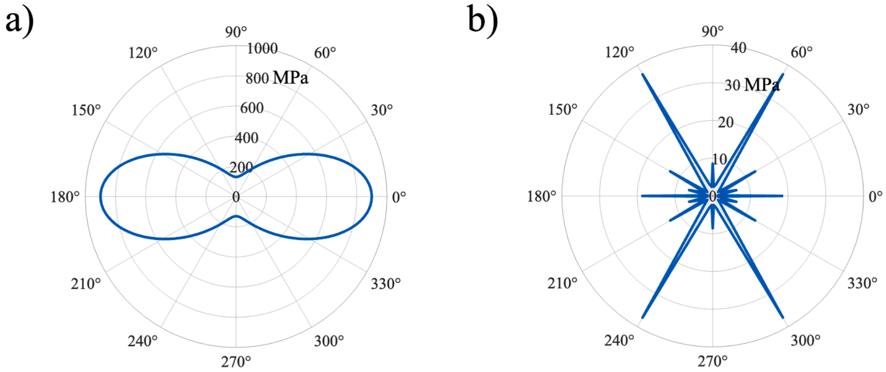

Fig. D1. CRSS (in MPa units) as a function of orientation for pure Ni from: (a) original P-N model (b) present method. Note that the original P-N model gives stress levels near 1000 MPa while the current model provides CRSS levels less than 40 MPa.

requiring a non-planar description of the core structure [62,63]. The model does not rely on any empirical parameters and provides a method for the CRSS that captures the characteristics of a dislocation with an arbitrary character. The extended dislocation is described by four parameters, specifically the core widths of the Shockley partials (ξ_{TP} and ξ_{LP}) and the individual positions of these partials (s_1 and s_2). These parameters are determined from an energy minimization method that incorporates the elastic and misfit energies of dislocations and finds the optimum parameters that minimize the total energy. The elastic energy is obtained by utilizing the fully anisotropic E-S framework. The strain fields are calculated to obtain the correct strain energy density for the interaction yielding the accurate anisotropic interaction coefficient for the elastic energy calculations. The core energy of the dislocation is computed by the novel WS-M approach that accounts for the actual atomic positions on the slip plane. Thus, the proposed framework presents an accurate determination of the energy components of a general extended dislocation, advancing over existing approaches to the best of the authors' knowledge.

The behavior of the continuum strain-energy and the atomistic misfit energy is further elaborated below, using the isolated Shockley partial as an example. The analysis is performed for an isolated partial so that the coupled effect due to the other partial is eliminated. The variation of both the strain-energy $E_{STRAIN-SP}(\xi_{SP})$ and the misfit-energy $E_{MISFIT-SP}(\xi_{SP})$ for an isolated Shockley partial as a function of its core-width ξ_{SP} are schematically illustrated in Fig. 7. As a general rule, dislocation has a wider core (e.g., ξ_2) if the edge component is more dominant than the screw component since the edge component tends to widen the core to reduce its high elastic energy. This is due to the fact that the infinitesimal fractions within the dislocation core are spaced out further at higher core-widths, reducing their repulsive energy of interaction. Consequently, the strain-energy $E_{STRAIN-SP}$ reduces with increasing core-width and the misfit energy $E_{MISFIT-SP}$ behaves in a contrasting manner. At low core-width (e.g., ξ_1), the misfit within the core is concentrated in a smaller region, and thus exhibits low misfit energy. Conversely, at high core-width, the misfit is more spread out on the slip plane, increasing the total misfit energy. Thus, the misfit energy increases with core-width in direct contrast with the strain-energy. A minimum of the total energy E_{TOT} is achieved at an optimal balance between the two energies. The corresponding core-width is the equilibrium core-width of the dislocation.

The varying character of a dislocation is closely related to the changing atomic arrangements on the slip plane with respect to the dislocation line direction. This is illustrated in Fig. 8 for different scenarios showing the crystal orientation of the slip plane for screw, 60°, and edge cases. The dashed arrow shows the direction of the Burgers vector of the full dislocation which in combination with the dislocation line direction decides the character as quantified by the angle θ shown in Fig. 9. Notice that, the orientation of the W-S cell domain area changes with character and so does the integration limits, which play a critical role in the spatial misfit energy summation given in Eq. (13). The effect of changing lattice is internalized by the key quantity, a_{norm}, as defined in Section 2.2.2. a_{norm} is effectively linked to the interplanar spacing along the direction dislocation moves. Thus, it has a direct connection to the periodicity of the energy trajectory that is passed through by the dislocation. The relevance of this parameter, a_{norm}, is demonstrated more vividly in Fig. 8 (b) by the close correlation between the CRSS and a_{norm} vs. character. Although a_{norm} is closely linked to the observed CRSS value, that itself is not sufficient to predict the correct CRSS as the correlation is not direct and affected by other properties involved in the analysis. Note that, a_{norm} is the largest for the screw and 60° cases creating a larger barrier for slip. The 60° case is especially critical as it has the highest CRSS amongst all the characters and as a mixed dislocation, it has asymmetric density distribution which also contributes to its CRSS. Al is an exception to this behavior mainly because of the undissociated structure of the screw dislocation as obtained from the present analysis. The results for Al and comparison with the literature is provided in Appendix C. The non-trivial dependence of the CRSS on dislocation character is an outcome of the complex interplay between the material properties and the crystallography as captured with the present analysis. Previous studies recognized the non-symmetric dislocation density distributions and limited number of them noted the non-monotonic variation of CRSS with character to the best of authors' knowledge [64,65]. However, the current framework differs from these approaches primarily because of the novel W-S cell based misfit-energy integration.

Another crucial advantage of the developed framework is the capacity to selectively analyze the effect of fault energetics on the CRSS, without the effect of elastic constants. Information of such nature is critical in conceiving how sensitive the CRSS is to the unstable and stable stacking fault energy barriers. For this analysis, the elastic constants of FeNiCoCrMn are employed and maintained constant while the fault energies are varied. The character is fixed at 60° as it is shown to have the highest CRSS amongst all characters, thus useful in predicting the overall yield strength of a material. Such a selective parametric study is only made possible by the availability of an analytical framework as proposed in this study. The underlying fault energy barriers are varied across a 16 × 16 grid of values and at each grid point, the core-parameters and CRSS values are determined. The results are plotted in Fig. 9 as a spline surface fit and the results for the shown materials are provided as a supplementary material. The strong role of the unstable fault energy γ_{us} is established. The sensitivity of dependence between the CRSS and the underlying core-width is dictated by γ_{us}. If γ_{us} is large, a small reduction in the core-widths can dramatically raise the CRSS, and vice versa. This barrier has a more dominant role than the intrinsic energy barrier γ_{isf} in dictating the CRSS. However, CRSS is also influenced by γ_{isf}, yielding an increased magnitude of CRSS for higher γ_{isf}. The reduced core-width is because the misfit energy associated with the intrinsic stacking fault between the partials drives the partials to have smaller cores in an effort to lower the misfit energy. For low γ_{isf} values, one can expect that this reduction would not be as significant. However, when the unstable energy γ_{us} is high, such a small reduction of width results in a dramatic increase in the CRSS as referred to before. The effect of varying γ_{isf} for materials with a relatively lower γ_{us} is shown more clearly by the plot showing the CRSS vs γ_{isf} at a fixed value of $\gamma_{\mathrm{us}} = 300\ \mathrm{mJ/m^2}$ in Fig. 9. There is a drastic increase in the CRSS with increasing γ_{isf}, thus we can conclude that the effect of increasing γ_{isf} is more significant for materials with a relatively lower γ_{us}. Thus, it is a non-trivial coupled effect between the γ_{us} and γ_{isf} fault energies of the partials that leads to the higher CRSS of the extended dislocation, τ_{F}. Such an explanation of the dependencies of CRSS on the underlying fault energies has not been made thus far to the best of the authors' knowledge and is a direct consequence of the developed analytical framework.

The intermittent motion of the partials to avoid higher energy peaks result in a fluctuation in SFW as shown in the Section 2.5. The amplitude of this fluctuation, denoted by Δd, is not unique and depends on material properties and dislocation characteristics. Fig. 10 illustrates the variation of Δd with the critical fault energy barriers, namely, unstable stacking fault energy γ_{us} and intrinsic stacking fault energy γ_{isf}. The elastic constants of FeNiCoCrMn are employed and maintained constant while the fault energies are varied, and the dislocation character is fixed at 60°. This zig-zag motion, schematically depicted in (i) and (ii), is more substantial in materials with a high γ_{us} and low γ_{isf}, which corresponds to the region where many high entropy alloys lie. For instance, for FeNiCoCrMn Δd is higher than b_P implying a more substantial intermittent motion of the partials. Further, for the majority of pure elements, this effect is relatively modest. Despite that, even a small fluctuation in stacking fault width is crucial for avoiding higher energy peaks to yield a lower CRSS closer to the experimental observations. Thus, the present analysis is essential in predicting the CRSS values more accurately.

Regarding the model for high entropy alloy cases, we note that our CRSS formulation relies on the fault energies associated with multi-elements on the slip plane (in our case the Wigner-Seitz lattice). We are calculating the lattice resistance of 60° and screw dislocation for Cantor alloy as 178 MPa and 147 MPa respectively, in general agreement with the experiments (172 MPa) on single crystals [46]. The range of CRSS (145-175 MPa) has been confirmed in other experimental works and reviews [47,66,67] as well. Our results show that an additional solute hardening contribution term for the screw and 60° cases, beyond the role of multi-elements in modifying the GSFE curves, may not be necessary. For the edge case, we calculate CRSS of 13.75 MPa, a rather low lattice resistance. If we did not seek the maximum lattice resistance orientation, one could argue that solute hardening must substantially contribute to CRSS based on consideration of the edge case alone. Twinning can activate at stress levels close to slip in FeNiCoCrMn, hence extra care must be taken for differentiating slip from twinning in experiments [46]. Another material where single crystal data is available is NiCoCr with a CRSS value of 140 MPa [68], and the GSFE calculations give a negative SFE [69–71]. Short Range Order (SRO) effect was ruled out in one study [72] while it was discussed as a major contributing factor in others [51,73]. So, the debate on the strengthening contributions continues. We emphasize that one must evaluate the lattice resistance as a baseline prior to attributing other contributions. We will show in a later publication that finite width of correct magnitude and correct CRSS are predicted based on our lattice resistance calculations on NiCoCr accounting for the dislocation character effects.

4. Conclusions

The present study establishes a predictive analytical framework for CRSS calculation of extended dislocation in FCC materials with an arbitrary character and all the inputs to the model can be obtained from first-principles calculations. The following critical remarks can be deduced,

1. An extension to the Wigner-Seitz-Cell-Misfit (WS-M) model is established that is capable of analyzing dislocations with arbitrary characters incorporating the actual atomic arrangements on the two-dimensional slip-plane of the lattice for any chosen character.
2. The variation of core-widths, SFW and CRSS values across the entire spectrum of characters between the screw and edge nature are presented. It is shown that the CRSS of the dislocation can exhibit a maximum at a non-trivial mixed character that is neither edge nor screw, depending upon the elastic anisotropy and the fault energetics of the material.
3. The proposed framework is further utilized to reveal the complex dependencies of the CRSS on the underlying fault energies, namely the unstable stacking fault energy γ_{us} and intrinsic stacking fault energy γ_{isf}. It is shown that both energy barriers exhibit a coupled influence to elevate the CRSS of the extended dislocation.
4. The individual behaviors of strain and misfit energies are elaborated using the isolated partial case as an example. The trend with varying core-width is elucidated revealing that the minimum total energy is achieved with the contribution from both energy components.
5. The Minimum-Energy-Path (MEP) for the dislocation motion exhibits an intermittent motion of partials implying a fluctuation in the stacking fault width during motion. The amplitude of this fluctuation is strongly controlled by the fault energy barriers and shown to be

higher for materials with high unstable stacking fault energy γ_{us} and low intrinsic stacking fault energy γ_{isf} barriers.

6. The challenging case of pure Al was analyzed, and the stacking fault widths were predicted as zero for pure screw case and 6.05 Å and 7.65 Å for 60° and pure edge cases respectively in agreement with experiments.

Declaration of Competing Interest

The authors declare that they have no known competing financial interests or personal relationships that could have appeared to influence the work reported in this paper.

Acknowledgments

The work is supported by the National Science Foundation (NSF) grant under award number CMMI-21-25821 and partly by the Air Force Office of Scientific Research (AFOSR) under award number FA9550–22-1-0314, which is gratefully acknowledged. The use of the Illinois Campus Cluster, a computing resource that is operated by the Illinois Campus Cluster Program (ICCP) in conjunction with the National Center for Supercomputing Applications (NCSA) and which is supported by funds from the University of Illinois at Urbana-Champaign, is also gratefully acknowledged. We thank the reviewers on further discussion of high entropy alloys, the complexity of pure aluminum, and explaining the classical Stroh method versus the current study. The assistance of Mr. Daegun You on the aluminum simulations is gratefully acknowledged.

Supplementary materials

Supplementary material associated with this article can be found, in the online version, at doi:10.1016/j.actamat.2023.118982.

Appendix A: Calculation of the elastic interaction coefficients

A brief description of the E-S formalism is provided here, and the reader is referred to [31] for a more detailed explanation of the analysis. Using this framework, the displacement field, u, for a dislocation with arbitrary Burgers vector, $\overrightarrow{b}$, is analytically expressed as,

$$u_i(x_1, x_2) = \frac{1}{2\pi\sqrt{-1}} \sum_{\alpha=1}^{6} \eta_\alpha A_{i\alpha} L_{s\alpha} b_s \ln(x_1 + p_\alpha x_2) \tag{A.1}$$

where $\eta_\alpha = 1$ for $\alpha \in \{1,2,3\}$ and $\eta_\alpha = -1$ for $\alpha \in \{4,5,6\}$, and $\{p_\alpha, A_{i\alpha}, L_{s\alpha}\}$ are the E-S constants. The E-S constants are determined from the equations:

$$\| \; C_{ijkm}(\delta_{i1} + p_\alpha \delta_{i2})(\delta_{m1} + p_\alpha \delta_{m2}) \; \| = 0 \tag{A.2}$$

$$C_{ijkm}(\delta_{i1} + p_\alpha \delta_{i2})(\delta_{m1} + p_\alpha \delta_{m2}) A_{k\alpha} = 0 \tag{A.3}$$

$$L_{j\alpha} = -\delta_{i2} C_{ijkm}(\delta_{m1} + p_\alpha \delta_{m2}) A_{k\alpha} \tag{A.4}$$

where C_{ijkm} is the anisotropic elastic tensor in the $x_1 - x_2 - x_3$ coordinate system and δ_{ij} is the Kronecker delta function. The elastic constants of the FCC materials considered in this study are listed in Table 4. Then, the strain-field is calculated using the relation,

$$\varepsilon_{ij} = \frac{1}{2}\left(\frac{\partial u_i}{\partial x_j} + \frac{\partial u_j}{\partial x_i}\right) \tag{A.5}$$

Thus, the strain-field in terms of computed E-S constants is expressed as,

$$\varepsilon_{ij}(x_1, x_2) = \frac{1}{4\pi\sqrt{-1}} \sum_{\alpha=1}^{6} \frac{\eta_\alpha L_{s\alpha} b_s}{(x_1 + p_\alpha x_2)} \left(A_{i\alpha}\left(\delta_{1j} + p_\alpha \delta_{2j}\right) + A_{j\alpha}\left(\delta_{1i} + p_\alpha \delta_{2i}\right)\right) \tag{A.6}$$

The current analysis involves two distinct Burgers vectors, $\overrightarrow{b}_{TP}$ and $\overrightarrow{b}_{LP}$, forming the extended dislocation. These partials can have different characters and, hence, must be treated individually. Thus, the anisotropic E-S constants are computed separately for these partials, which are utilized to compute the strain-fields corresponding to trailing and leading partials, $\varepsilon_{ij}^{TP}(x_1, x_2)$ and $\varepsilon_{ij}^{LP}(x_1, x_2)$ respectively, from the equations (A.1-A.6). The core-region within radius $r_0 = 5b_P$ around the center of each partial is excluded as continuum formalism does not hold in this core region where the strains are large. The superposition of these individual strain-fields yields the total net strain-field expressed as,

$$\varepsilon_{ij}(x_1, x_2, R) = \varepsilon_{ij}^{TP}(x_1 + R/2, x_2) + \varepsilon_{ij}^{LP}(x_1 - R/2, x_2) \tag{A.7}$$

where $(0, -R/2)$ is the position of the trailing partial and $(0, R/2)$ is the position of the leading partial as schematically depicted in Fig. A.1. Subsequently, the strain energy density distribution corresponding to the net strain field created due to the two partials is obtained as,

$$e_{el}(x_1, x_2, R) = \frac{1}{2} C_{abcd} \varepsilon_{ab}(x_1, x_2, R) \varepsilon_{cd}(x_1, x_2, R) \tag{A.8}$$

where C_{abcd} is the anisotropic elastic tensor in the $x_1 - x_2 - x_3$ coordinate system. Consequently, the strain-energy per unit length of the dislocation line is computed by integrating the spatial strain-energy density distribution, e_{el}, expressed as,

$$E_{\perp-\perp}(R)=\int_{-X_{\max}}^{X_{\max}}\int_{-X_{\max}}^{X_{\max}} e_{el}(x_1,x_2,R)dx_1dx_2 \tag{A.9}$$

The integral in eqn. A.9 is computed numerically, over a discretized grid employing a sufficiently fine grid size $(\Delta x_1/b_P=\Delta x_2/b_P\approx 0.2)$ and large limit of integration $(X_{\max}=150b_P)$ for convergence. Finally, the equation capturing the variation in total strain-energy with the separation distance is expressed as,

$$E_{\perp-\perp}\left(\overrightarrow{b}_{LP},\overrightarrow{b}_{TP},R\right)=C_0+K_{12}\frac{\left|\overrightarrow{b}_{LP}.\overrightarrow{b}_{TP}\right|}{2\pi}\ln R \tag{A.10}$$

where C_0 is the constant and K_{12} is the anisotropic interaction coefficient. Note that, $E_{\perp-\perp}(R)$ varies linearly with $(\ln R)$ as plotted in Fig. A.1 for three cases with different dislocation characters. The linear trend seen in Fig. A.1 is independent of the selection of R. It is clear that if one uses larger R values, the integration limits should be increased accordingly and the coefficient K_{12} remains the same. Thus, K_{12} is determined from the slope of the curve and utilized to capture the elastic interaction between the partials. Similarly, the self interaction coefficients for the trailing and leading partials, K_{11} and K_{22}, are determined by repeating the procedure by considering the interaction between two dislocations with same Burgers vectors ($\overrightarrow{b}_{LP}$ or $\overrightarrow{b}_{TP}$).

Appendix B: Comparison of two methods for interaction coefficient calculation

In this appendix, we compare two methods for calculating interaction energy of a dislocation. The K interaction coefficients denote the coefficients determined in this study. On the other hand, the self-energy coefficient (henceforth named K^E to distinguish) is to be obtained from the Stroh method [31]. The self-energy coefficient K^E is pertinent in the calculation of total-energy of a single Volterra dislocation inside an anisotropic medium. However, in this study, the interaction coefficient K is pertinent to the interaction energy between two dislocations within an anisotropic medium. Computing this interaction coefficient, K, involves the determination of strain-energy of two dislocations $E_{\perp-\perp}(R)$ as a function of the distance of separation between them, R.

Consider the example of the "11" component: The interaction coefficient K_{11} is employed to determine the interaction energy between identical dislocations with the same Burgers vectors $\overrightarrow{b}_{LP}$ located within an anisotropic medium with a separation distance R between them. On the other hand, the Stroh self-energy coefficient K^E_{11} is the pre-factor to one of the summands in the self-energy equation involving the 1st component of the Burgers vector $\overrightarrow{b}_{LP}$.

Expressing the above distinction in terms of equations, present method computes,

$$E_{\perp-\perp}\left(\overrightarrow{b}_{LP},R\right)=C_0+K_{11}\frac{\left|\overrightarrow{b}_{LP}.\overrightarrow{b}_{TP}\right|}{2\pi}\ln R \tag{B.1}$$

which is analogous to Eq. (7) in the manuscript. Letting $G_{11}=K_{11}\frac{|\overrightarrow{b}_{LP}.\overrightarrow{b}_{TP}|}{2\pi}$ and rewriting Eq. (B.1) we obtain,

$$E_{\perp-\perp}\left(\overrightarrow{b}_{LP},R\right)=C_0+G_{11}\ln R \tag{B.2}$$

where G_{11} is the prelogarithmic energy factor obtained from the current method. Whereas the Stroh method uses the coefficients K^E_{ij} to determine the self-energy of a single dislocation within an anisotropic medium as [31,74],

$$E^{STROH}\left(\overrightarrow{b}_{LP}\right)=\left(\frac{K^E_{11}}{2\pi}\left(\overrightarrow{b}_{LP}.\widehat{e}_1\right)\left(\overrightarrow{b}_{LP}.\widehat{e}_1\right)+\frac{K^E_{12}}{2\pi}\left(\overrightarrow{b}_{LP}.\widehat{e}_1\right)\left(\overrightarrow{b}_{LP}.\widehat{e}_2\right)+\ldots\right)\ln\frac{R_{outer}}{r_0} \tag{B.3}$$

where $\widehat{e}_i$ $(i=1,2,3)$ are the unit orthonormal vectors along the coordinate system axes $x_1-x_2-x_3$ and R_{outer}, r_0 being the outer and inner cutoff radii, respectively.K^E is the inverse of the matrix F, whose elements are,

$$F_{ij}=\sum_{\alpha=1}^{3}\left(A_{i\alpha}M_{\alpha j}+A_{j\alpha}M_{\alpha i}\right) \tag{B.4}$$

where M is the inverse of L which is obtained from Eq. (A.4).

Hence, for a dislocation with Burgers vector $\overrightarrow{b}$, Eq. (B.3) is expressed as,

$$E^{STROH}\left(\overrightarrow{b}\right)=\frac{K^E_{ij}b_ib_j}{2\pi}\ln\frac{R_{outer}}{r_0} \tag{B.5}$$

Letting $G^E=\frac{K^E_{ij}b_ib_j}{2\pi}$, the Eq. (B.5) can be rewritten as,

$$E^{STROH}\left(\overrightarrow{b}\right)=G^E\ln\frac{R_{outer}}{r_0} \tag{B.6}$$

where G^E is the prelogarithmic energy factor for a single Volterra dislocation.

For the quantitative comparison of interaction coefficients of these two approaches, we present the results for Ni and FeNiCoCrMn in Table B1. Additionally, we provide the values for prelogarithmic energy factors, G and G^{STROH} computed from both methods in Table B2.

The two energies $E_{\perp-\perp}$ and E^{STROH} are computing physically different strain-energies and only the former computation is relevant in this study to determine the correct core-widths. Only through the calculation of the interaction coefficients K_{ij} in our study can the variation of strain-energy with changing core-widths be captured accurately. Thus, the original Stroh calculation is not applicable to the current problem. Since these two energies and corresponding K-coefficients are distinct, one cannot replace $K_{12}\left|\overrightarrow{b}_{LP}.\overrightarrow{b}_{TP}\right|$ in Eq. (B.1) with an expression involving Stroh-coefficients of the form $K_{ij}^E b_i b_j$.

We would like to point out that the equilibrium core-width strongly depends on the elastic interaction coefficient and small deviations in core-width can significantly affect the calculated CRSS. This has been a major issue in the field for CRSS determination as this sensitivity to core-width necessitates a precise determination of the core-width. The isotropic assumption results in significant errors in the magnitude of core-width and consequently in CRSS calculations even if it were to capture the behavioral trend of core-width versus character. Therefore, an anisotropic calculation as proposed in this study is necessary. To illustrate this, we summarize the results obtained by employing both methods in Table B3.

Appendix C: Results for Al and comparison with the literature

Regarding the model capabilities we offer the following comments on separation of partials and dislocation cores widths (see Table C1).

Separation of Partials

For pure Al, in our study, the highest CRSS is observed for the screw character, and we obtain a stable minimum in our total energy curve at zero separation width (undissociated), i.e., $d = 0$ Å and this observation is in agreement with experiments [79]. Also, for the screw case, we predict a dislocation core width of 2.83 Å and a corresponding CRSS of 88 MPa. There are experimental findings that point to such high CRSS values at low temperatures and various experimental findings are reviewed in [76]. In agreement with our result, no dissociation of partials was noted for screw dislocation in Al [76,82] and this case results in high CRSS levels widely known in experiments. In contrast, other works predict a finite separation width [64,65,77,78,83] not observed in TEM experiments [79,80]. Interestingly, in [76] the possibility of finite separations for the screw case, though not common, was raised. We do predict such a clear metastable point in energy at 3.5 Å (not absolute minimum) (also discussed in [76]) with potentially higher CRSS values (125 MPa). This points to the need for extreme care in simulations for small stacking fault widths. On the other hand, for the case of edge dislocations the separation width in Al in our study is finite (7.65 Å) which is in close agreement to experimental studies of 8 Å [79]. We predict a CRSS of 13.9 MPa for the edge case with symmetric partial core widths. Also, for the 60° case, we predict a stacking fault separation of 6.05 Å which is also in close agreement with reported experimental SFW of 5.5 Å [81] confirming the capability of the current model.

Dislocation Core Widths

To assess the CRSS model, one must also check two fundamental quantities: (a) the magnitude of the core-widths, and (b) the asymmetry of the core-widths among the partials. Regarding (a), the magnitude of the core-widths varies widely in the literature, say for aluminum [64,65,77,78]. This is partly due to the potentials and partly due to the simulation methodology (boundary conditions, simulation size, and elastic strain energy calculations and treatment of anisotropy) used. The non-symmetric dislocation core-widths for the 60° case are predicted as (3.9 Å, 2.8 Å) in our model. We predicted (3.53 Å, 3.53 Å) for the edge case for the partials and (2.83 Å, 2.83 Å) for the screw case. The dislocation density distributions for screw, 60°, and edge cases are given in Fig. C1. The dislocation core widths are difficult to measure experimentally compared to stacking fault widths; also, many of the simulations do not provide them. Regarding (b), we make two points: (1) the mixed character cases must result in non-symmetric leading and trailing partial core widths. On the other hand, (2) it is necessary to have symmetric core widths for the screw and pure edge characters which is not obeyed in some of the previous works [65]. Such results are crucial to assess the theory and simulations [65]. As stated above, in most works, the core widths are not provided [64,76,78], and would facilitate better comparisons among different studies in the future.

Appendix D: Comparison of character dependence of CRSS between the original P-N model and the current approach

The original P-N method yields [6,20,54],

$$\sigma_P = 2\kappa \exp\left(-\frac{4\pi\xi(\theta)}{b_F} \right) \tag{D.1}$$

where σ_P is the friction stress calculated from the original P-N model, $\kappa = \mu\{cos^2(\theta) + [1/(1-\nu)]sin^2(\theta)\}$, $\xi(\theta) = \frac{\kappa d}{2\mu}$ is the core-width of the dislocation, d is the interplanar spacing of the $\{111\}$ planes and b_F is the Burgers vector magnitude. For Ni, we take $\mu = 76$ GPa and $\nu = 0.31$ [84]. These results are compared in Fig. D1. Fig. D1 (a) provides the original P-N model and Fig. D1 (b) provides current model results.

References

[1] R. Asaro, V. Lubarda, Mechanics of solids and materials, Cambridge University Press, 2006.

[2] F. Roters, P. Eisenlohr, T.R. Bieler, D. Raabe, Crystal plasticity finite element methods: in materials science and engineering, John Wiley & Sons, 2011.

[3] P.B. Chowdhury, H. Sehitoglu, R.G. Rateick, H.J. Maier, Modeling fatigue crack growth resistance of nanocrystalline alloys, Acta Materialia 61 (7) (2013) 2531–2547.

[4] R. Pippan, The condition for the cyclic plastic deformation of the crack tip: the influence of dislocation obstacles, International Journal of Fracture 58 (4) (1992) 305–318.

[5] J.R. Rice, R. Thomson, Ductile versus brittle behaviour of crystals, The Philosophical Magazine: A, Journal of Theoretical Experimental and Applied Physics 29 (1) (1974) 73–97.

[6] B. Joós, M.S. Duesbery, The Peierls Stress of Dislocations: An Analytic Formula, Physical Review Letters 78 (2) (1997) 266–269.

[7] G. Schoeck, The Peierls model: Progress and limitations, Materials Science and Engineering: A 400-401 (2005) 7–17.

[8] Y. Shen, X. Cheng, Dislocation movement over the Peierls barrier in the semi-discrete variational Peierls framework, Scripta Materialia 61 (5) (2009) 457–460.

[9] G. Liu, X. Cheng, J. Wang, K. Chen, Y. Shen, Peierls stress in face-centered-cubic metals predicted from an improved semi-discrete variation Peierls-Nabarro model, Scripta Materialia 120 (2016) 94–97.

[10] V.V. Bulatov, E. Kaxiras, Semidiscrete Variational Peierls Framework for Dislocation Core Properties, Physical Review Letters 78 (22) (1997) 4221–4224.

[11] H. Yu, S. Cao, S.S. Youssef, Y.-J. Ma, J.-F. Lei, Y. Qi, Q.-M. Hu, R. Yang, Generalized stacking fault energies and critical resolved shear stresses of random α-Ti-Al alloys from first-principles calculations, Journal of Alloys and Compounds 850 (2021), 156314.

[12] Y. Kamimura, K. Edagawa, A.M. Iskandarov, M. Osawa, Y. Umeno, S. Takeuchi, Peierls stresses estimated via the Peierls-Nabarro model using ab-initio γ-surface and their comparison with experiments, Acta Materialia 148 (2018) 355–362.

[13] F.R.N. Nabarro, Dislocations in a simple cubic lattice, Proceedings of the Physical Society 59 (2) (1947) 256–272.

[14] R. Peierls, The size of a dislocation, Proceedings of the Physical Society 52 (1) (1940) 34–37.

[15] J.N. Wang, A new modification of the formulation of Peierls stress, Acta Materialia 44 (4) (1996) 1541–1546.

[16] V.A. Lubarda, X. Markenscoff, Variable core model and the Peierls stress for the mixed (screw-edge) dislocation, Applied Physics Letters 89 (15) (2006), 151923.

[17] L.C. Lim, R. Raj, Continuity of slip screw and mixed crystal dislocations across bicrystals of nickel at 573 K, Acta Metallurgica 33 (8) (1985) 1577–1583.

[18] P.M.J. Marée, J.C. Barbour, J.F.v.d. Veen, K.L. Kavanagh, C.W.T. Bulle-Lieuwma, M.P.A. Viegers, Generation of misfit dislocations in semiconductors, Journal of Applied Physics 62 (11) (1987) 4413–4420.

[19] T.M. Smith, M.S. Hooshmand, B.D. Esser, F. Otto, D.W. McComb, E.P. George, M. Ghazisaeidi, M.J. Mills, Atomic-scale characterization and modeling of 60° dislocations in a high-entropy alloy, Acta Materialia 110 (2016) 352–363.

[20] J.P. Hirth, J. Lothe, Theory of Dislocations (2nd ed.), Journal of Applied Mechanics 50 (2) (1983) 476–477.

[21] F.A. McClintock, A.S. Argon, Mechanical behavior of materials, Addison-Wesley Pub. Co., Reading, Mass, 1966.

[22] V. Vítek, Intrinsic stacking faults in body-centred cubic crystals, The Philosophical Magazine: A, Journal of Theoretical Experimental and Applied Physics 18 (154) (1968) 773–786.

[23] B. Joós, Q. Ren, M.S. Duesbery, Peierls-Nabarro model of dislocations in silicon with generalized stacking-fault restoring forces, Physical Review B 50 (9) (1994) 5890–5898.

[24] X. Li, S. Schönecker, W. Li, L.K. Varga, D.L. Irving, L. Vitos, Tensile and shear loading of four fcc high-entropy alloys: A first-principles study, Physical Review B 97 (9) (2018) 94102. -94102.

[25] D.C. Chrzan, M.P. Sherburne, Y. Hanlumyuang, T. Li, J.W. Morris, Spreading of dislocation cores in elastically anisotropic body-centered-cubic materials: The case of gum metal, Physical Review B 82 (18) (2010), 184202. -184202.

[26] Y. Kamimura, K. Edagawa, S. Takeuchi, Experimental evaluation of the Peierls stresses in a variety of crystals and their relation to the crystal structure, Acta Materialia 61 (1) (2013) 294–309.

[27] H.B. Huntington, Modification of the Peierls-Nabarro Model for Edge Dislocation Core, Proceedings of the Physical Society. Section B 68 (12) (1955) 1043–1048.

[28] A.S.K. Mohammed, O.K. Celebi, H. Sehitoglu, Critical stress prediction upon accurate dislocation core description, Acta Materialia 233 (2022), 117989.

[29] D. You, O.K. Celebi, A.S.K. Mohammed, D.W. Abueidda, S. Koric, H. Sehitoglu, CRSS determination combining ab-initio framework and Surrogate Neural Networks, International Journal of Plasticity 162 (2023) 103524.

[30] D.M. Barnett, J. Lothe, An image force theorem for dislocations in anisotropic bicrystals, Journal of Physics F: Metal Physics 4 (10) (1974) 1618–1635.

[31] A.N. Stroh, Dislocations and Cracks in Anisotropic Elasticity, The Philosophical Magazine: A, Journal of Theoretical Experimental and Applied Physics 3 (30) (1958) 625–646.

[32] S. Kibey, J.B. Liu, D.D. Johnson, H. Sehitoglu, Predicting twinning stress in fcc metals: Linking twin-energy pathways to twin nucleation, Acta Materialia 55 (20) (2007) 6843–6851.

[33] S.M. Collard, R.B. McLellan, High-temperature elastic constants of platinum single crystals, Acta Metallurgica et Materialia 40 (4) (1992) 699–702.

[34] J.R. Neighbours, C.S. Smith, The elastic constants of copper alloys, Acta Metallurgica 2 (4) (1954) 591–596.

[35] S. Gene, W. Herbert, Single crystal elastic constants and calculated aggregate properties, MIT, Cambridge, MA, 1971.

[36] J. Bandyopadhyay, K.P. Gupta, Low temperature lattice parameter of nickel and some nickel-cobalt alloys and Grüneisen parameter of nickel, Cryogenics 17 (6) (1977) 345–347.

[37] O.K. Celebi, A.S.K. Mohammed, J.A. Krogstad, H. Sehitoglu, Evolving dislocation cores at Twin Boundaries: Theory of CRSS Elevation, International Journal of Plasticity 148 (2022), 103141.

[38] H.J. Leamy, H. Warlimont, The Elastic Behaviour of Ni-Co Alloys, physica status solidi (b) 37 (2) (1970) 523–534.

[39] S. Alkan, A. Ojha, H. Sehitoglu, Determination of latent hardening response for FeNiCoCrMn for twin-twin interactions, Acta Materialia 147 (2018) 149–164.

[40] S. Kibey, J.B. Liu, M.J. Curtis, D.D. Johnson, H. Sehitoglu, Effect of nitrogen on generalized stacking fault energy and stacking fault widths in high nitrogen steels, Acta Materialia 54 (11) (2006) 2991–3001.

[41] P. Söderlind, J.A. Moriarty, J.M. Wills, First-principles theory of iron up to earth-core pressures: Structural, vibrational, and elastic properties, Physical Review B 53 (21) (1996) 14063–14072.

[42] J.N. Wang, Prediction of Peierls stresses for different crystals, Materials Science and Engineering: A 206 (2) (1996) 259–269.

[43] G. Schoeck, The Peierls dislocation: Line energy, line tension, dissociation and deviation, Acta Materialia 45 (6) (1997) 2597–2605.

[44] A.J. Foreman, M.A. Jaswon, J.K. Wood, Factors Controlling Dislocation Widths, Proceedings of the Physical Society. Section A 64 (2) (1951) 156–163.

[45] B.A. Szajewski, A. Hunter, D.J. Luscher, I.J. Beyerlein, The influence of anisotropy on the core structure of Shockley partial dislocations within FCC materials, Modelling and Simulation in, Materials Science and Engineering 26 (1) (2018), 015010.

[46] W. Abuzaid, H. Sehitoglu, Critical resolved shear stress for slip and twin nucleation in single crystalline FeNiCoCrMn high entropy alloy, Materials Characterization 129 (2017) 288–299.

[47] E.P. George, W.A. Curtin, C.C. Tasan, High entropy alloys: A focused review of mechanical properties and deformation mechanisms, Acta Materialia 188 (2020) 435–474.

[48] P.S. Venkatesan, D.N. Beshers, Internal Friction Studies in Nickel Crystals from 77° to 298°K, Journal of Applied Physics 41 (1) (1970) 42–49.

[49] C. Varvenne, G.P.M. Leyson, M. Ghazisaeidi, W.A. Curtin, Solute strengthening in random alloys, Acta Materialia 124 (2017) 660–683.

[50] M. Shih, J. Miao, M. Mills, M. Ghazisaeidi, Stacking fault energy in concentrated alloys, Nature Communications 12 (1) (2021) 3590.

[51] R. Zhang, S. Zhao, J. Ding, Y. Chong, T. Jia, C. Ophus, M. Asta, R.O. Ritchie, A. M. Minor, Short-range order and its impact on the CrCoNi medium-entropy alloy, Nature 581 (7808) (2020) 283–287.

[52] H. Conrad, S. Frederick, The effect of temperature and strain rate on the flow stress of iron, Acta Metallurgica 10 (11) (1962) 1013–1020.

[53] U.F. Kocks, A.S. Argon, M.F. Ashby, Thermodynamics and Kinetics of Slip, Pergamon Press, 1975.

[54] J.P. Simmons, S.I. Rao, D.M. Dimiduk, Atomistics simulations of structures and properties of $\frac{1}{2}\langle 110\rangle$ dislocations using three different embedded-atom method potentials fit to γ-TiAl, Philosophical Magazine A 75 (5) (1997) 1299–1328.

[55] C. Varvenne, A. Luque, W.A. Curtin, Theory of strengthening in fcc high entropy alloys, Acta Materialia 118 (2016) 164–176.

[56] G. Laplanche, A. Kostka, C. Reinhart, J. Hunfeld, G. Eggeler, E.P. George, Reasons for the superior mechanical properties of medium-entropy CrCoNi compared to high-entropy CrMnFeCoNi, Acta Materialia 128 (2017) 292–303.

[57] C.B. Carter, S.M. Holmes, The stacking-fault energy of nickel, The Philosophical Magazine: A, Journal of Theoretical Experimental and Applied Physics 35 (5) (1977) 1161–1172.

[58] P. Kwasniak, H. Garbacz, K.J. Kurzydlowski, Solid solution strengthening of hexagonal titanium alloys: Restoring forces and stacking faults calculated from first principles, Acta Materialia 102 (2016) 304–314.

[59] M. Ghazisaeidi, D.R. Trinkle, Core structure of a screw dislocation in Ti from density functional theory and classical potentials, Acta Materialia 60 (3) (2012) 1287–1292.

[60] B. Yin, Z. Wu, W.A. Curtin, Comprehensive first-principles study of stable stacking faults in hcp metals, Acta Materialia 123 (2017) 223–234.

[61] D. Rodney, L. Ventelon, E. Clouet, L. Pizzagalli, F. Willaime, Ab initio modeling of dislocation core properties in metals and semiconductors, Acta Materialia 124 (2017) 633–659.

[62] V. Vitek, M. Mrovec, J. Bassani, Influence of non-glide stresses on plastic flow: from atomistic to continuum modeling, Materials Science and Engineering: A 365 (1-2) (2004) 31–37.

[63] R. Gröger, Which stresses affect the glide of screw dislocations in bcc metals? Philosophical Magazine 94 (18) (2014) 2021–2030.

[64] D.L. Olmsted, K.Y. Hardikar, R. Phillips, Lattice resistance and Peierls stress in finite size atomistic dislocation simulations, Modelling and Simulation in, Materials Science and Engineering 9 (3) (2001) 215.

[65] G. Lu, N. Kioussis, V.V. Bulatov, E. Kaxiras, Generalized-stacking-fault energy surface and dislocation properties of aluminum, Physical Review B 62 (5) (2000) 3099–3108.

[66] L. Patriarca, A. Ojha, H. Sehitoglu, Y.I. Chumlyakov, Slip nucleation in single crystal FeNiCoCrMn high entropy alloy, Scripta Materialia 112 (2016) 54–57.

[67] I.V. Kireeva, Y.I. Chumlyakov, Z.V. Pobedennaya, A.V. Vyrodova, I. Karaman, Twinning in [001]-oriented single crystals of CoCrFeMnNi high-entropy alloy at tensile deformation, Materials Science and Engineering: A 713 (2018) 253–259.

[68] W. Abuzaid, L. Patriarca, A study on slip activation for a coarse-grained and single crystalline CoCrNi medium entropy alloy, Intermetallics 117 (2020), 106682.

[69] S. Zhao, G.M. Stocks, Y. Zhang, Stacking fault energies of face-centered cubic concentrated solid solution alloys, Acta Materialia 134 (2017) 334–345.

[70] S. Zhao, Y. Osetsky, G.M. Stocks, Y. Zhang, Local-environment dependence of stacking fault energies in concentrated solid-solution alloys, npj, Computational Materials 5 (1) (2019) 13.

[71] J. Ding, Q. Yu, M. Asta, R.O. Ritchie, Tunable stacking fault energies by tailoring local chemical order in CrCoNi medium-entropy alloys, Proceedings of the National Academy of Sciences 115 (36) (2018) 8919–8924.

[72] B. Yin, S. Yoshida, N. Tsuji, W.A. Curtin, Yield strength and misfit volumes of NiCoCr and implications for short-range-order, Nature Communications 11 (1) (2020) 2507.

[73] J. Ding, Q. Yu, M. Asta, R.O. Ritchie, Tunable stacking fault energies by tailoring local chemical order in CrCoNi medium-entropy alloys, Proc Natl Acad Sci U S A 115 (36) (2018) 8919–8924.

[74] D.J. Bacon, D.M. Barnett, R.O. Scattergood, Anisotropic continuum theory of lattice defects, Progress in Materials Science 23 (1980) 51–262.

[75] G. Schoeck, The core structure of dislocations in Al: a critical assessment, Materials Science and Engineering: A 333 (1-2) (2002) 390–396.

[76] I. Shin, E.A. Carter, Possible origin of the discrepancy in Peierls stresses of fcc metals: First-principles simulations of dislocation mobility in aluminum, Physical Review B 88 (6) (2013).

[77] S. Xu, J.R. Mianroodi, A. Hunter, B. Svendsen, I.J. Beyerlein, Comparative modeling of the disregistry and Peierls stress for dissociated edge and screw dislocations in Al, International Journal of Plasticity 129 (2020), 102689.

[78] C. Woodward, D.R. Trinkle, L.G. Hector, D.L. Olmsted, Prediction of Dislocation Cores in Aluminum from Density Functional Theory, Physical Review Letters 100 (4) (2008), 045507.

[79] W. Höllerbauer, H. Karnthaler, Beitr. elektonenmicr, Direktabb. Oberfl 14 (1981) 361.

[80] T. Waitz, Private Communication, University of Vienna, 2023.

[81] M.J. Mills, P. Stadelmann, A study of the structure of Lomer and 60° dislocations in aluminium using high-resolution transmission electron microscopy, Philosophical Magazine A 60 (3) (1989) 355–384.

[82] G. Schoeck, The core structure of dislocations in Al: a critical assessment, Materials Science and Engineering: A 333 (1) (2002) 390–396.

[83] Y. Mishin, D. Farkas, M.J. Mehl, D.A. Papaconstantopoulos, Interatomic potentials for monoatomic metals from experimental data and ab initio calculations, Physical Review B 59 (5) (1999) 3393–3407.

[84] W. Köster, H. Franz, Poisson's ratio for metals and alloys, Metallurgical Reviews 6 (1) (1961) 1–56.